Variation in tissue correction factors for LiF, Al_2O_3 and Silicon Dosimeters as a function of tissue depth with comparison between intensity weighted mono-energetic photon and the poly-energetic photons used in brachytherapy and diagnostic radiology.

A thesis submitted in partial
Fulfillment of the requirements for the degree of
Doctor of Philosphy

By

Sashi Poudel

August 2017
Worcester Polytechnic Institute

This thesis is approved for recommendation to the Graduate committee.

_____

Dr. David Medich
Thesis Director

_____ _____

Dr. Germano Innachinone
Committee Member

Dr.Izabela Stroe
Committee Member

_____

Dr. Marco Kaltofen
External Committee Member

ABSTRACT

The MCNP6 radiation transport code was used to quantify changes in the absorbed dose tissue conversion factors for LiF, Al_2O_3, and silicon-based electronic dosimeters. While normally calibrated in-air and applied to all general geometric measurements, tissue conversion factors for each dosimeter were obtained at various depths in a simulated water phantom and compared against the standard in-air calibration method.

In these experiments, a mono-energetic photon source was modeled at energies between 30 keV and 300 keV for a point-source placed at the center of a water phantom, a point-source placed at the surface of the phantom, and for a 10-cm radial field geometry. Again, mono-energetic photon source was modeled up to 1300 keV for a disk-source placed at the surface of the phantom and dosimetric calculations were obtained for water, LiF, Al_2O_3, and silicon at depths of 1 mm to 35 cm from the source. The dosimeter's absorbed dose conversion factor was calculated as a ratio of the absorbed dose to water to that of the dosimeter measured at a specified phantom depth. The dosimeter's calibration value also was obtained for both mono and polyenergetic source and the calibration value from poly-energetic source was compared with the intensity weighted average calibration value from mono-energetic photon.

The calculated changes in the tissue conversion factors are significant because the American Association of Physicists in Medicine (AAPM) recommend that measurements of a brachytherapy

or diagnostic source be made with an overall uncertainity of 5% or better. Yet, based on results, the absorbed dose tissue conversion factor for a LiF dosimeter was found to deviate from its calibration value by up to 9%, an Al_2O_3 dosimeter by 43%, and a silicon dosimeter by 61%. These uncertainties are in addition to the normal measurement uncertainties.

By applying these tissue correction factors, these data may be used to meet the AAPM measurement requirements for mono-energetic and poly-energetic sources at measurement depths up to 35 cm under the irradiation geometries investigated herein.

ACKNOWLEDGEMENTS

I first wish to thank my graduate advisor Dr. David Medich who welcomed me in the world of medical physics, outlined my path in it, guided and supervised thoroughly in every step of this work. Without his support, my graduate studies would not have been as enjoyable or as successful. I look forward to staying in touch in coming years and maintaining a lifelong friendship.

Secondly, I would like to thank the rest of my thesis committee: Dr. Germano Iannacchione, Dr. Izabela Stroe, and Dr. Marco Kaltofen for their support and insightful comments. Thank you Prof. Innachione for writing all the requested reference letters for my job interviews. I would like to thank entire WPI physics department faculty for their help and guidance during my TA days.

I also thank my fellow labmates Danielle, Nick, Shawn, Andrew, Norbert and all the members of Medich Lab of Radiation for all the fun we had. I would like to thank our physics department staff Roger, Jackie, Fred, Michelle and Peg for their help during my initial days. And my sincere thanks also go to Dr. Clayton French, Dr. Mark Tries from Umass Lowell (UML) and Dr. Blake Currier because without their support my UML graduate studies would not have been successful.

Finally, I would like to thank my parents: Hem lal Sharma and Narbada Poudel, Brothers: Mr and Mrs Devi Poudel and Mr. and Mrs. Amrit Poudel, Sister Manju Poudel and kids: Bishal, Bibek, Manisha and Mahendra.

TABLE OF CONTENTS

LIST OF FIGURES

Fig 2.4: Glow curve at a dose of 14.6 mGy for LiF: Mg, Cu, P.

Figure: 2.5: A survival curve using the standard LQ formula $e^{-(\alpha D+\beta D2)}$ where $\alpha = 0.2$ and $\alpha/\beta = 3$. The components of cell killing are equal where the curves $e^{-\alpha D}$ and $e^{-\beta D2}$ intersect. This occurs at dose $D = \alpha/\beta$ (3 Gy in this example).

Figure 2.6: Increase in cancer risk by age, BEIR VII Phase 2 Report.

Figure 2.7: Particle interaction histories.

Figure 2.8: Example MCNP regions.

Figure 4.1: Percent deviation of the dosimeter's CF relative to an in-air calibration value for LiF at distances of 1 cm, 3 cm, 5 cm, and 10 cm in a water phantom. These dosimetric values represent the response from a monoenergetic point-source located at the center of a pseudo-infinite water phantom.

Figure 4.2: Al_2O_3, percent deviation of the dosimeter's CF relative to an in-air calibration value at 1 cm, 3 cm, 5 cm, and 10 cm depths in a water phantom for a point-source located at the surface of a pseudo-infinite water phantom.

Figure 4.3: Silicon percent deviation in CF relative to an in-air calibration value for a mono-energetic field source impinging normally on the surface of the water phantom. In this study, the field was modeled to have a radius of 10 cm. In this figure, the authors' selected 5% significant deviation level is depicted as a horizontal dashed line.

Figure 4.4: LiF percent deviation of the dosimeter's CF relative to an in-air calibration value at 1 cm, 3 cm, 5 cm, and 10 cm depths in a water phantom for a point-source located at the surface of a pseudo-infinite water phantom.

Figure 4.5: Al percent deviation of the dosimeter's CF relative to an in-air calibration value at 1 cm, 3 cm, 5 cm, and 10 cm depths in a water phantom for a point-source located at the surface of a pseudo-infinite water phantom.

Figure 4.6: Silicon percent deviation of the dosimeter's CF relative to an in-air calibration value at 1 cm, 3 cm, 5 cm, and 10 cm depths in a water phantom for a point-source located at the surface of a pseudo-infinite water phantom.

Figure 4.7: LiF percent deviation of the dosimeter's CF relative to an in-air calibration value at 1 cm, 3 cm, 5 cm, and 10 cm depths in a water phantom for a point-source and Field source.

Figure 4.8: Al percent deviation of the dosimeter's CF relative to an in-air calibration value at 1 cm, 3 cm, 5 cm, and 10 cm depths in a water phantom for a point-source and Field source.

Figure 4.9: Si percent deviation of the dosimeter's CF relative to an in-air calibration value at 1 cm, 3 cm, 5 cm, and 10 cm depths in a water phantom for a point-source and Field source.

Figure 4.10: Percent deviation of the dosimeter's CF relative to an in-air calibration value for LiF distances of 1 cm, 8 cm, 17 cm, 26 cm and 34cm in a water phantom. These dosimetric values represent the response from a monoenergetic disk-source located at the surface of a pseudo-infinite water phantom.

Figure 4.11: Percent deviation of the dosimeter's CF relative to an in-air calibration value for Al distances of 1 cm, 8 cm, 17 cm, 26 cm and 34cm in a water phantom. These dosimetric values represent the response from a monoenergetic disk-source located at the surface of a pseudo-infinite water phantom.

Figure 4.12: Percent deviation of the dosimeter's CF relative to an in-air calibration value for Si distances of 1 cm, 8 cm, 17 cm, 26 cm and 34cm in a water phantom. These dosimetric values represent the response from a monoenergetic disk-source located at the surface of a pseudo-infinite water phantom.

Fig 4.13: Comparison of Tissue correction factor between polyenergetic photon source Yb-169 and the weighted TCF from the monoenergetic sources for LiF dosimeter.

Fig 4.14: Comparison of Tissue correction factor between polyenergetic photon source Yb-169 and the weighted TCF from the monoenergetic sources for al_2O_3 dosimeter.

Fig 4.15: Comparison of Tissue correction factor between polyenergetic photon source Yb-169 and the weighted TCF from the monoenergetic sources for Si dosimeter.

Fig 4.16: Comparison of Tissue correction factor between polyenergetic photon source Ir-192 and the weighted TCF from the monoenergetic sources LiF dosimeter.

Fig 4.17: Comparison of Tissue correction factor between polyenergetic photon source Ir-192 and the weighted TCF from the monoenergetic sources for al_2O_3 dosimeter.

Fig 4.18: Comparison of Tissue correction factor between polyenergetic photon source Ir-192 and the weighted TCF from the monoenergetic sources for Si dosimeter.

LIST OF TABLES

1. INTRODUCTION

Unlike a direct dosimeter, such as a calorimeter[1] or a Fricke dosimeter, most radiation detectors commonly used to measure radiation absorbed dose must be calibrated against a well characterized field of radiation to convert the absorbed dose deposited in a dosimeter, $D_{dosimeter}$ into the more relevant absorbed dose to tissue. Because water and tissue have similar electron-density and because water has a well-defined chemical composition, most dosimeters are calibrated to measure absorbed dose to water, D_{H2O}. Yet obtaining a precise measurement of the absorbed dose in a high-gradient field, such as that produced by a brachytherapy source or diagnostic X-ray field, can be difficult since the dosimeter must have excellent spatial resolution, must be water equivalent, and preferably must be able to measure low radiation absorbed doses.

Under such constraints, researchers commonly use LiF thermoluminescent dosimeters [TLDs] [2] which have an effective atomic number calculated [3] to be $Z_{eff}(LiF) = 8.3$, electronic dosimeters, [4] which can be modeled as elemental silicon [$Z(Si) = 14$], and more recently, Al_2O_3 optically stimulated luminescent dosimeters, [OSLs] [5] which have an effective atomic number $Z_{eff}(Al_2O_3) = 11.3$. By design, these dosimeters have a higher atomic number than that of water [$Z_{eff}(H_2O) = 7.5$] [6] which increases that detector's dosimetric sensitivity relative to water. Unfortunately, this increased sensitivity also causes the detector to have an energy-dependent photon response relative to water that especially becomes important at photon energies between 30 keV and 300 keV. This energy dependence primarily is caused by differences in photoelectric absorption, which is a primary interaction mechanism for photons at these energies and which depends strongly [7] with both atomic number (Z) and incident photon energy (E) as $\sigma \propto Z^4 * E^{-3}$. The photoelectric effect

therefore causes low and mid-energy (≤ 300 keV) photons to have a strong material and energy dependent interaction mechanism. Above about 300 keV, the photoelectric absorption probability becomes negligible compared with the Compton interaction probability and this energy-material dependence phenomena becomes less important; this is because the Compton interaction probability only is mildly material and energy dependent [7].

Consider how the energy and material dependence of low and mid-energy photons could influence a dosimetric measurement in a highly scattering environment, such as a water phantom. As photons are Compton-scattered in the phantom, the average energy of the resulting (scattered plus primary) photon fluence decreases which increases the probability of photoelectric absorption. Because low and mid-energy photons have an energy and material dependent response, the ratio between the absorbed doses deposited in a dosimeter relative to that of water will not remain constant; this is the basis for the observed energy dependence of a dosimeter.

For the simplistic case of mono-energetic source photons transported under conditions of charged particle equilibrium (CPE), the absorbed dose deposited in the active region of a dosimeter can be obtained theoretically [8] as:

$$D(r)_{CPE} = \Phi(r) \cdot E_\gamma \cdot \left[\frac{\mu_{en}}{\rho}\right]_{med} = \psi(r,E) \cdot \left[\frac{\mu_{en}}{\rho}\right]_{med}. \quad (1)$$

Here, *D(r)* represents the absorbed dose deposited to a specified material, $\Phi(r)$ is photon fluence in unit of cm^{-2}, E_γ is the photon energy in MeV, $[\mu_{en/\rho}]_{med}$ is the mass energy absorption coefficient ($cm^2 \cdot g^{-1}$) of the absorbing medium, and $\psi(r,E)$ is the photon energy fluence (MeV$\cdot$ cm^{-2}).

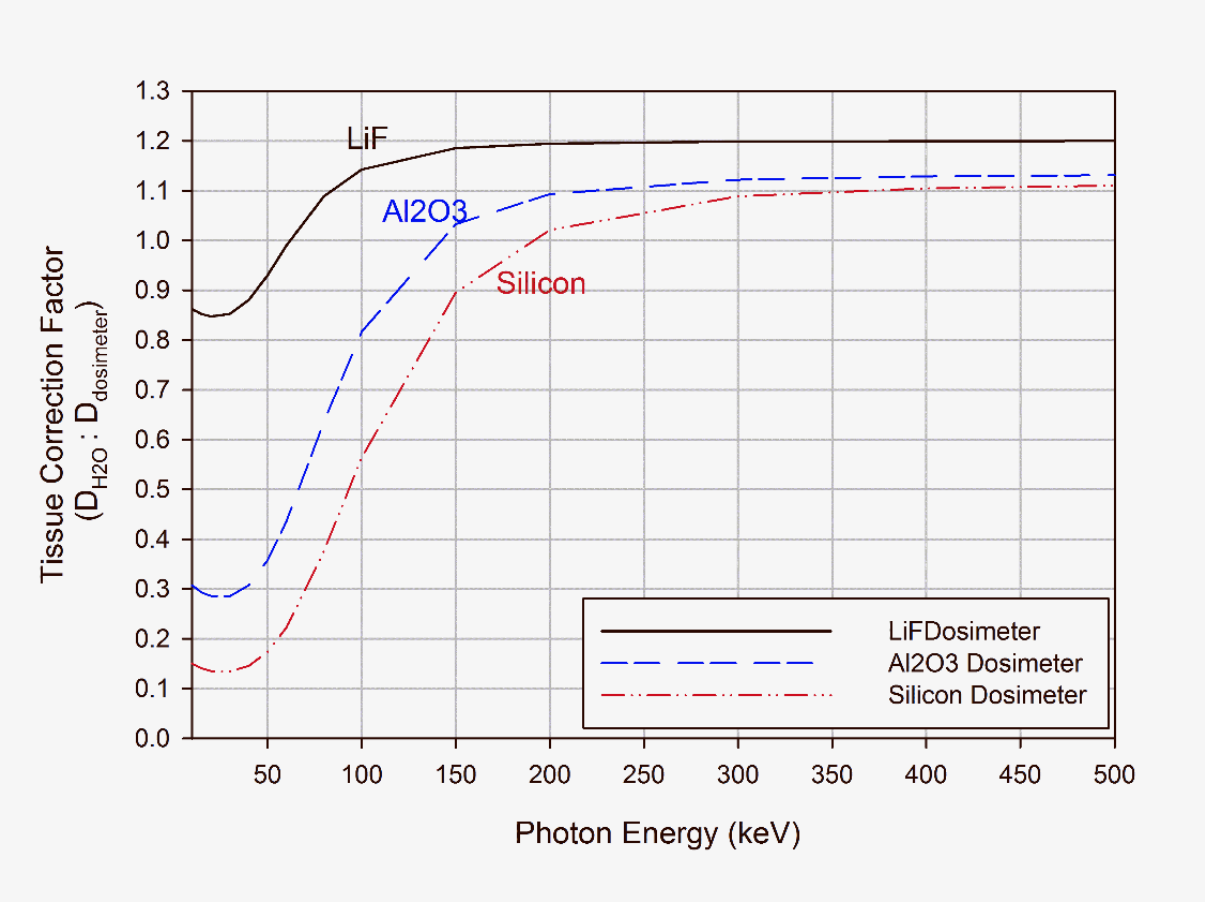

Figure 1.1: Calculated change in the dosimeter calibration value as a function of photon energy for LiF, Al_2O_3, and silicon-based dosimeters.

A dosimeter's absorbed dose conversion factor (CF), which is used to convert the absorbed dose measured by a detector into the absorbed dose to water, can be calculated as the ratio of the two absorbed doses as shown in Eq. 2 below.

$$f(r)_{Dosimeter->H_2O} = \frac{D(r)_{H_2O}}{D(r)_{Dosimeter}}. \quad (2)$$

For the specific case where these absorbed dose measurements are made under conditions of negligible photon scatter and from a known and well-characterized photon source (for example, a

mono-energetic point-source), the CF is called the dosimeter's *calibration value*, that is, the dosimeter becomes "calibrated" for that source type. By combining Eq. 1 with Eq. 2, the CF under conditions of CPE can be simplified to be the ratio of mass energy absorption coefficients for water to that of the dosimeter material as demonstrated in Eq. 3.

$$f(r)_{Dosimeter->H_2O} = \frac{\Phi(E_\gamma) \cdot E_\gamma \cdot [\frac{\mu_{en}}{\rho}]_{H_2O}}{\Phi(E_\gamma) \cdot E_\gamma \cdot [\frac{\mu_{en}}{\rho}]_{Dosimeter}} = \frac{[\frac{\mu_{en}}{\rho}]_{H_2O}}{[\frac{\mu_{en}}{\rho}]_{Dosimeter}}. \quad (3)$$

Based on Eq. 3, the calibration value for LiF, Al_2O_3, and silicon were calculated for exposure to mono-energetic photons with energies between 30 and 300 keV. The values of the mass energy absorption coefficients used in these calculations were obtained from NIST [9] and the results presented in Fig. 1. In this figure, the dosimeter's calibration value is observed to change by 42% for LiF, 300% for Al_2O_3, and 740% for Si as the photon energy is increased from 30 keV to 300 keV. This variation is important because calibrated dosimeters often are placed in a strong scattering medium, such as a water phantom, and that dosimeter's calibration value then is used to predict the absorbed dose to water. Yet, because the population of scattered photons detected by the dosimeter increases as a function of depth in the phantom, the average energy of the photon fluence incident on the detector will decrease, which could cause the CF to deviate significantly from its expected (calibration) value for a low-mid energy photon source.

Therefore, the author performed a Monte Carlo study to quantify the change in the absorbed dose CF for LiF, Al_2O_3, and silicon dosimeters placed in a water phantom under three irradiation geometries. These geometries include: 1) a point-source located at the center of a pseudo-infinite [10] water phantom, 2) a point-source located at the surface of a pseudo-infinite water phantom,

and 3) a 10 cm radial field impinging on the surface of a water phantom. Dosimetric data were obtained at phantom depths between 0.2 and 10 cm after irradiation from a photon source designed to emit mono-energetic photons with energies between 30 and 300 keV.

For reference, the author has selected a 5% deviation between the detector's measured CF and calibration value to be statistically significant. This value was selected based on the precision of a well-characterized LiF TLD, which is approximately 7% at low doses [11], and based on the AAPM Technical Guidance Document 56 [12] which recommends that the total uncertainty in a brachytherapy source dosimetric characterization be no more than 5 to 10% for clinical use.

Ytterbium-169 is a mid-energy brachytherapy source. It is produced in a nuclear reactor by neutron activation of Yb-168 in ytterbium oxice (Yb_2O_3) powder via Yb-168 (n,y)Yb-169, and decays with a half life of 32 days by electron capture to stable thulium (Tm-169)[13]. Yb-168 has a natural abudance of just 0.13%, but the high thermal neutron capture cross-section and its availability in enriched form ($\leq$ 20%) allow for very high specific activity of up to 10 Ci/mm^3. As a result, Yb-169 is appropriagte for HDR brachytherapy application and various designs of Yb-169 sources have been described in the published literature[14, 15]. The relatively low energy photon spectrum of Yb-169 is not only attractive for dose enhancement but also add multiple advantage including the possibility of in-vivo shielding of essential organs and tissues. This property of Yb-169 has clinical applications. With only 0.25 mm of lead shielding required to reduce the intensity of a point-source by a factor of 2 (the HVL1), the Yb-169 source could be shielded locally using a small amount of shielding material (high Z material) thus reducing radiation exposure to personnel, simplified HDR room shielding, streamlined after-loading units, and overall reduce costs.

The Yb-169 photon spectrum, presented in fig 1, primarily constists of photons between 49.5 to 307.7 keV. In this spectrum of the photons, majority of the photons have energies is less than 100 keV. The photons having energies less than 100 keV absorbed in high Z material is called photoelectric interaction.

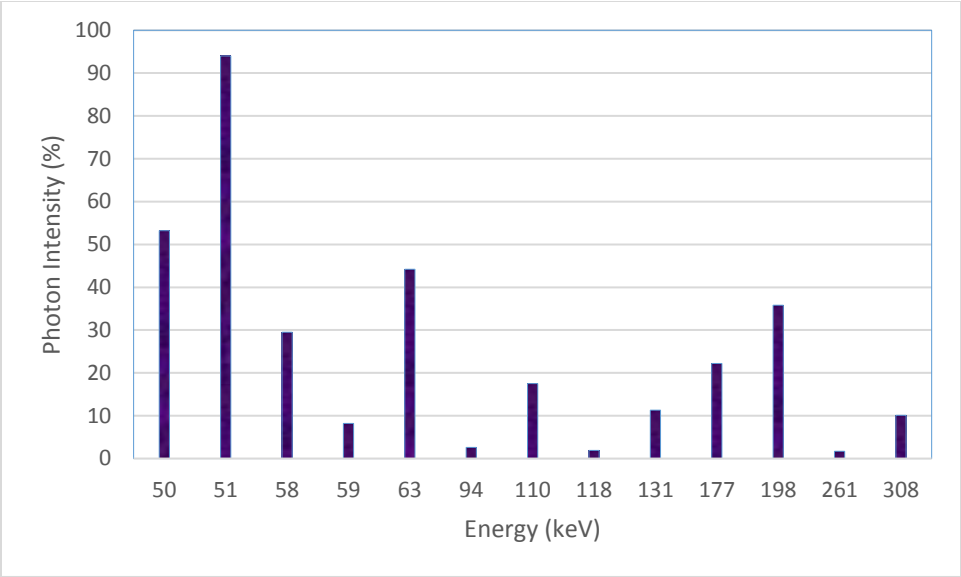

Figure 1.2: Histogram representation of the theoretical Yb-169 photon spectrum. Yb-169 also emits photons with energies between 320 and 781 keV but are not shown in the histogram because of their small relative intensity (less than 0.1%).

Table 1.1: Photon energies, intensity and uncertainity for Yb-169

Energy (KeV)	Intensity	Uncertainty (%)
49.5	0.532	2.50
50.7	0.940	2.30
57.6	0.295	2.50
59.1	0.082	2.70
63.1	0.442	0.60
93.6	0.026	0.04
109.8	0.175	0.18
118.2	0.019	0.01
130.5	0.113	0.09

177.2	0.222	0.18
198.0	0.358	0.30
261.1	0.017	0.001
307.7	0.101	0.011

The average energy of this spectrum is 92.7 keV, the total intenisity is 332.09% and the total weighte uncertainty is 1.5%. Yb-169 has a half life of 32.026 days.The total photon yield for the Yb-169 is 3.222; this yiled was used in the calculation of the dose in the tally region.

Iridium-192 is a standard high-dose-rate brachytherapy source which has been studied and tested for clinical treatments of lungs, esophageal, prostrate, cervical, coronary, and other cancers[16]. It is produced by thermal neutron capture form the stable Ir-191 via Ir-191 (n,y) Ir-192, and decays with a half life of 74 days by beta and gamma emmision to stable thulium (Pt-192). The beta rays emitted present energy ranging form 530 keV to 670 keV, and the main gamma rays emitted have an average energy of 370 keV. Iridium-191 has a high absorption section for neutrons (910 barns)[17]. These sources are usually shaped as flexible wires with 0.3mm and 0.5mm diameter and can be easily cut in the length requested for each application[18] The specific activity, for a low dose rate (LDR) therapy, is between 1mCi/cm and 4mCi/cm, being the main requested characteristic the activity homogeneity along the wire, not presenting a variation larger than 5% in a 50cm long wire[19].These wires comprise a Platinum-Iridium alloy core (80/20), encapsulated in a Platinum or Stainless Steel tube[20]. The coating aims to filter the low energy beta rays. Brachytherapy treatment can be carried out singly or associated to other techniques. The implants are made for several types of tumors, namely: oral cavity, cervix, breast, brain, skin, prostrate, eye, and others[21]. Among some specific Brachytherapy advantages[21] over the external radiation sources, the capacity to give form to the isodose distribution in irregular lesions, the considerable diminishing of dose outside the implant area (saving normal tissues) and the treatment quickness

can be highlighted. The Ir-192 photon spectrum, presented in fig 3.2, primarily constist of photons between 60 to 700 keV.

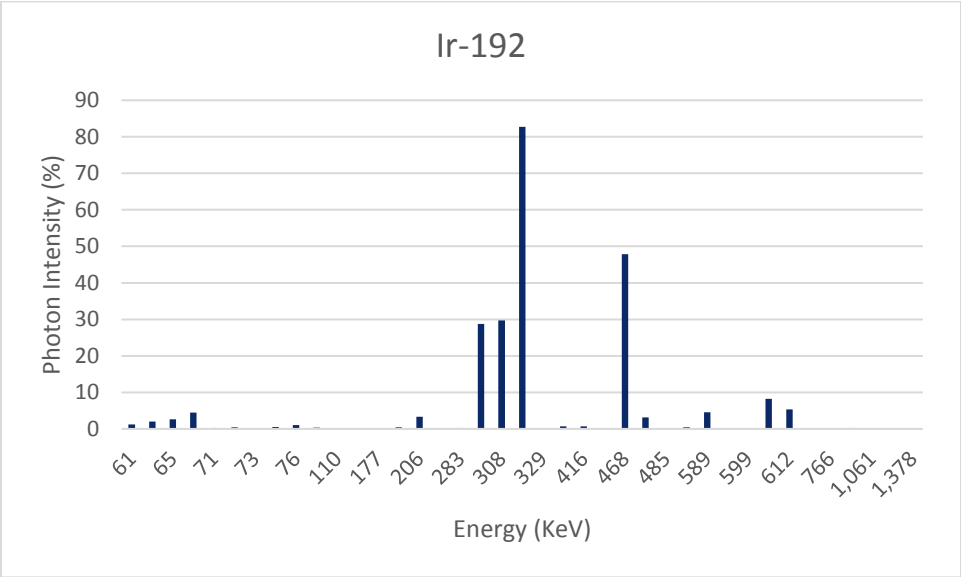

Figure 1.3: Histogram representation of the theoretical Ir-192 photon spectrum.

Table 1.2: Photon energies, intensity and uncertainity for Ir-192

Energy (KeV)	Probability (%)
61.4	1.2
63	2.05
65.122	2.63
66.831	4.46
71.079	0.24
71.414	0.46
73.363	0.16
75.368	0.53
75.749	1.02
77.831	0.36
110.4	0.01
136.343	0.2

176.98	0.004
201.311	0.47
205.794	3.34
280.27	0.009
283.267	0.266
295.957	28.72
308.455	29.68
316.506	82.71
329.17	0.0174
374.485	0.726
416.469	0.669
420.52	0.069
468.069	47.81
484.575	3.187
485.3	0.0023
489.06	0.438
588.581	4.517
593.49	0.0421
599.41	0.0039
604.411	8.2
612.462	5.34
703.87	0.0053
765.8	0.0013
884.537	0.291
1061.48	0.053
1089.9	0.0012
1378.2	0.0012

2. BACKGROUND

Energy emitted from a source is generally known to as radiation. Ionizing radiation is a radiation with enough energy capable of removing bound electrons from the orbit of an atom, leaving the atom to become charged or ionized. Ionization radiation occurs in two forms: waves or particles. Particulate radiation for example atomic and sub atomic particles carry energy in the form of kinetic energy while electromagnetic radiations carry energy in the form of osciallating electric and magnetic fields travelling throught space.

Charged particles for examples alpha particles and beta particles are considered directly ionizing because they can interact with atomic electrons through coulombic forces. Neutrons being chargeless can't interact with atomic electrons and are considered as indirectly charged particle. Like neutrons, gamma and X-rays are also electrically neutral and do not interact with orbital electrons directly. In this chapter, the typical types of X-ray interactions in diagnostic radiology and brachetherapy will be introduced, as well as radiation dosimetric quantities and radiation measurement devices.

2.1 X-ray interaction

X-rays are a form of electromagnetic raidiation composed of high-energy photons. Like all electromagnetic waves, the energy of a photon (E) is proportional to its frequency (ν), by a plank constant (h). This means that photon with low fewquencies, like radio waves, have lower energies than the photons with high frequencies, like X-rays.

$$E = hv \quad (1)$$

Ionizing radiation is a form of energy travelling either as electromagnetic waves (X-rays and gamma rays) or particles (alpha, beta neutrons etc.). When they interact with matter, their energy transfer to orbital electrons and these electrons lose energy by interacting with other electrons in adjacent atoms and produce ionizations. X-ray is categorized as indirect ionizing radiation. X-ray interaction with matter results in local energy deposition. There are mainly three types of interactions at the energy level of diagnostic X-ray[22]: Rayleigh scattering, Compton scatter, and Photoelectric effect.

A) Rayleigh scattering.

Rayleigh scattering occurs when a low-energy X-ray photon is scattered from an atom without any energy loss. There is no energy loss during this process but the direction of the scattered X-ray changes relative to the incident X-ray. This process does not contribute to dose but it does reduce the quality of image. It is more likely to happen when low energy photons are incident on high atomic number (Z) materials.

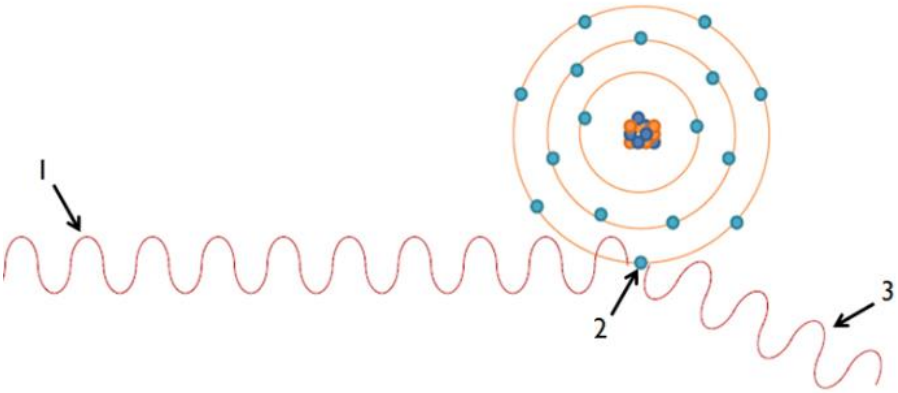

Fig 2.1 Rayleigh scattering: 1) An incoming x ray photon less than 10 keV interacts with an outer orbital electron. 2. The incoming x ray photon knocks the orbital electron out of it orbit. 3. Scattered photon with same energy.

B) Photoelectric Effect.

In the photoelectric effect, all of the incident photon energy is transferred to an atomic electron and gets ejected from the atom. Assuming the incident X-ray enegy E_0 and the binding energy of the electron E_b, the Kinetic energy E_e of the ejected electron is given by

$$E_e = E_0 - E_b \tag{2}$$

The condition for photoelectric absorption to occur is the incident photon must have energy greater than or equal to the binding energy of the electron. Following the photoelectric interaction, the atom is ionized, with an inner shell electron vacancy. The vacancy will be filled by an electron from higher energy level and the difference in energy is emitted as characteristic X-rays or Auger electrons. In diagnostic imaging, photoelectric effect is only important when the atomic number (Z) of the medium is high and the incident photon energy is just above the K edge energy.

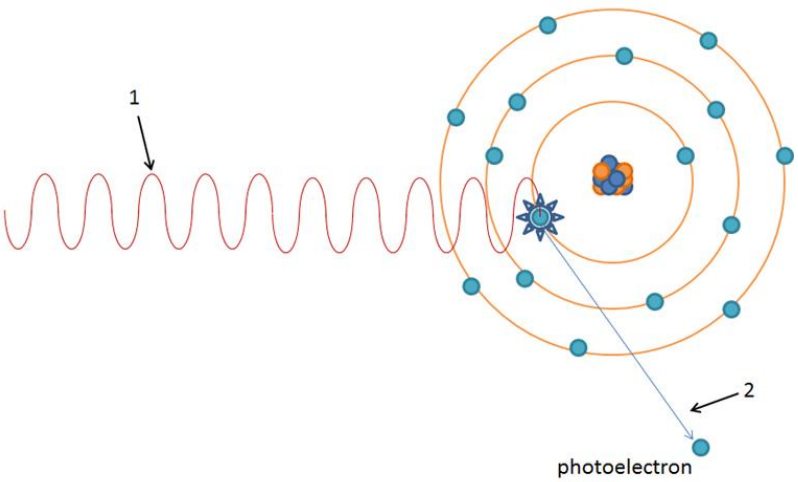

Fig 2.2 Photoelectric effect: 1. An incoming x ray photon knocks out an orbital electron (diagram show K shell electron being knocked out). 2. Photoelectron

C) Compton Scatterring.

Compton scattering is also called incoherent scattering and occurs between outer-shell electrons and incident X-ray photons. In this process, the electron is ejected from the atom, and the photon is scattered with reduced energy. Because both momentum and energy must be conserved, the incident energy (E_0) must be equal to the sum of the ejected electron energy (E_{e^-}) and energy of scattered phtons (E_{sc}). The relationship between scattering angle θ and the energies is described by following equation.

$$\frac{E_0}{E_{sc}} = 1 + \frac{E_0}{m_0 c^2}(1 - \cos\theta) \qquad (3)$$

Where E_{sc} = the energy of scattered photon,

E_0 = incident photon energy,

θ = the scattering angle.

The above equation (3) shows that the energy of scattered photon descrease with increasing scattering angle. Compton scattering is the dominant process among all scattering process in dioagnostic radiology.

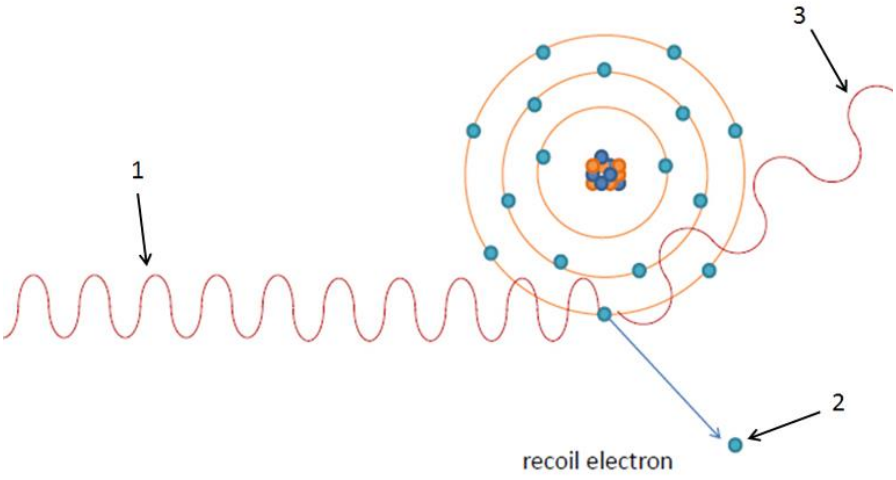

Figure 2.3: Compton Scattering: 1. An incoming X ray photon interacts with an outer orbital electron. 2. The incoming x ray photon knocks the orbital electron out of it orbit. 3. Scattered photon with reduced energy.

2.2 Radiation Dosimetry and Measurement

A) Exposure

Exposure is defined by the amount of electrical charge (ΔQ) produced by ionizing radiation per mass (Δm) of air.

$$Exposure = \frac{\Delta Q}{\Delta m} \tag{4}$$

The unit of exposure is Coulombs per kg. The historical unit of exposure is the roentgen (R) which is defined as 1 R = 2.58×10^{-4} Coulombs per kg. It is only defined for photons with energies less than 3 MeV and cannot be used for electrons, neutrons and protons[23]. In medical radiation dosimetry, exposure can be measured by placing an ion chamber directly in an X-ray beam. Exposure form x- ray source obeys the inverse square law and descrease with the square of the distance from a source.

B) Absorbed Radiation

Absorbed Dose

The absorbed dose (D) measures the amount of radiation energy (E) absorbed per unit mass (M) of a medium. It depends up on the material physical characteristics for given X-ray beam intensity. Material with high atomic number (Z) absorb more radiation energy than the ones with low atomic numbers. If a medium with mass M absorbs an energy of E, then the dose to the medium is

$$Dose = \frac{Radiation\ Energy\ (E)}{Mass\ (M)} = \frac{dE}{dM} \quad (5)$$

Absorbed dose is specified in grays (Gy) in the SI system and rad (radiation absorbed dose) in non-SI units. One gray is equal to 1 J of energy deposited per kilogram, and 1 rad is equal to 100 erg of energy deposited per gram.

The most useful absorbed dose quantities in radiology are skin doses and organ doses[24]. The organ doses are lower than the corresponding skin dose and depend on the X-ray beam quality and irradiation area.

Kerma

Photon interaction with matter takes place in two steps. First step is that it will transfers its energy to charged particles and the second is charged particles transfer energy directly though excitations and ionizations. The first step can be described as KERMA (kinetic energy released in material) and defined mathematically by,

$$Kerma = \frac{Radiation\ Energy\ Transfer\ (E_{tr})}{Mass\ (M)} = \frac{dE_{tr}}{dM} \tag{6}$$

And its relation to photon fluence is,

$$K = \varphi \cdot \left(\frac{\mu}{\rho}\right) \cdot \bar{E}_{tr} \tag{7}$$

Charge Particle Equilibrium

From the definition of kerma, it is the transfer of energy to the charged particles. But the most important point here is energy transfer and energy absorption will not take place at the same place[25]. There is a direct relation between kerma and fluence but the dose is calculated only in the assumption of charge particle equilibrium. Any volume is said to be in charge particle equilibrium if the number of charge particles leaving that volume is fulfilled by the the number of incoming charge particles. Under the condition of charge particle equilibrium, dose is equal to kerma and we can define dose mathematically as follows,

$$D = \varphi \cdot \left(\frac{\mu}{\rho}\right) \cdot \bar{E}_{ab} \quad (6)$$

Bragg-Gray Cavity Theory

Dose measurements are generally based on a measurement of charge produced through gas ionization[26].

$$D_{gas} = \frac{Q}{m_{gas}} \cdot W \quad (7)$$

Where, W – is the average energy required to cause one ionization in the gas and its value in air is 33.85 eV/ion pair.

Bragg- Gray cavity theory[27] can relate the dose in gas to the dose in the surrounding medium ("wall") through the ratio of mean stopping powers in gas and wall Bragg-Gray formula relates ionization in the gas cavity to absorbed dose in the medium[28, 29].

$$D_{wall} = \frac{Q}{m_{gas}} \cdot W \cdot \bar{\bar{S}}_{gas}^{wall} \quad (8)$$

Where $\bar{\bar{S}}_{gas}^{wall}$ designate averaging over both photon and electron spectra.

Equivalent Dose

Different types of radiation (ie α, β, γ, and X-ray) can result in different relative biological effectiveness (RBE)[30], which represents the biological harm caused by radiation. For example, a dose of 1 mGy deposited by alpha particle has greater RBE than the 1 mGy by X-ray photons. To account for the RBE, the equivalent dose H (unit: Sv) is defined as

$$H = D \times w_r \quad (9)$$

Where w_r is radiation weighting factor and D is the absorbed dose in the tissue.

Effective dose

Effective dose is designed to normalize the dose delivered to the irradiated body region to that of a whole-body exposure, and thus make risk estimation possible. The effective dose (E) is defined as

$$E = \sum_i w_i \times H_i \quad (10)$$

Where H_i is the equivalent dose to organ i and H_i is the tissue weighting factor which reprensents the relative radiosensitivity of the individual organ.

The summation in equation (7) is over all the organs and tissues irradiated for a specific examination. Effective dose is by far the best indicator of the patient radiatyion risk when doses to individual organs are below the threshold for the induction of deterministic effects.

B) Radiation Dosimeters

A radiation dosimeter is a device that measures of the energy aborbed per unit mass (absorbed dose) deposited in its sensitive volume by ionizing radiation. The most common dosimeters include film badge dosimeters, luminescence dosimeters and electronic dosimeters. Other commonly used ionizing radiation measuring devices include ionization chambers and Geiger counters.

Types of Dosimeters:

Direct Dosimeters: Direct reading dosimeters also called electronic dosimeters measure exposure in real time. These instruments are capable of showing immediate dose, dose rate and total dose. Semiconductor detectors, Ion chambers are the example of direct dosimeters.

Indirect Dosimeters: Indirect dosimeters also called passive dosimeters, are not capable of providing the real-time dose information to the users. Film badges, thermoluminescence dosimeters and optically stimulated luminescence dosimeters are the example of indirect dosimeters.

Film badge dosimeter:

Film badge dosimeters are the oldest type of dosimeter. A film badge contains a small film which is sensitive to radiation and when developed the exposed area increases its optical density in response to incident radiation. Here, the film dosimeter is read using a densitometer where the optical density of the developed film will be directly proportional to the radiation dose it has been exposed to. Film badge dosimeters can be worn under protective clothing and used to measure radiation doses received by radiation workers. However, the sensitivity of the film dependes up on the x ray photon energy.

Luminiscence Dosimetry:

Many crystalline materials emit light when either heated or stimulated with a visible light spectrum after exposure to ionizing radiation[25]. Thermoluniniscence dosimeters (TLDs) and optically stimulated luminescence dosimeters (OSLDs) are the examples of luminescence dosimetry and will be discussed here individually.

Thermoluminiscence dosimeter:

Thermoluminiscence dosimeters (TLDs) are passive dosimeters and have been replacing the film badges. They can store energy absorbed during X-ray exposure in electron traps, and trapped electron are released through a heating process as visible light. Lithium fluoride (LiF) is a typical TLD used in diagnostic radiology because of its effective atomic number close to the effective atomic number of the tissue. The detection limit of the TLD used to monitor radiation workers in diagnostic radiology is approximately[31] 0.3 mSv to 1 Sv.

The dose deposited in the TLD material can be determined using a TLD reader after the exposure. The TLD reader provides the stimulus heat to the chip material liberating trapped electrons which summarily emit optical photons as the electrons return to their stable state. The absorbed dose delivered to the TLD is determined by measuring the light intensity at various sample temperatures which creates a TLD glow curve[32].

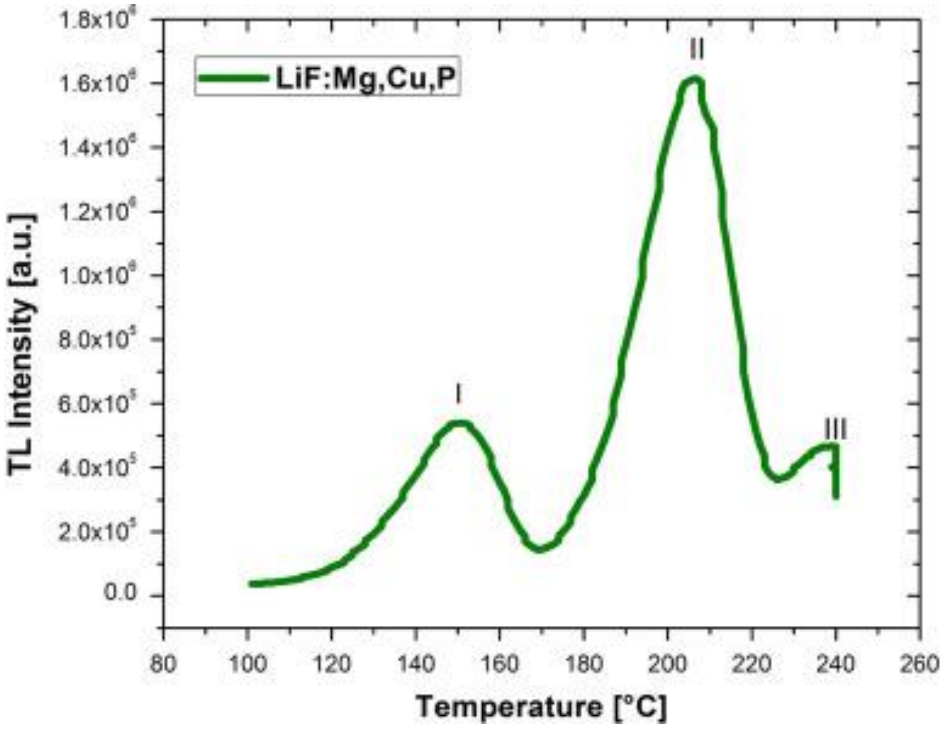

Fig 2.4: Glow curve at a dose of 14.6 mGy for LiF: Mg, Cu, P.

An optically stimulated luniniscence dosimeters (OSLDs) have a similar operating principle to TLDs, except that the readout is performed by stimulation by light instead of by heating. The material used for OSL are quartz, feldspars, and aluminium oxides. To produce OSL, the chip is excited with laser light through an optical fibre, and the resulting luminescence is carried back in the same fibre reflected through 90 degree by the beam splitter and measured in a PMT.The application of OSLs in medicine, including radiotherapy is slowly increasing.

Ionization chamber:

Ion chamber detect the ionizing radiation by measuring the electron charges liberated when X-ray photons ionize the gas inside the chamber. The Geiger counter is a kind of ionization chamber with a high voltage and provides "counts per minute". Geiger counter are sensitive and used to detect low level of radioactive contamination, but they don't tell the strength of radiation.

2.3 Radiobiology

Radiobiology is a branch of science concerned with the methods of interaction and the effects of ionizing radiation on living systems. When X-rays are absorbed in a living material, the energy absorbed is deposited in the tissues and cells and may cause related damage to individual cells or tissue. The total energy involved, however, can be relatively small. For example, a total body dose of ~4 Gy of X-rays given to a human is lethal in 60 days to about half of the individuals exposed. This dose represents an absorption of energy of only about 281 joule, which is equivalent to the amount of energy of raising body temperature of 0.002 ºC when converted to heat.

2.2.1 Radiation Exposure Effects on Molecular Level

On the molecular level, the main biological effects caused by radiation exposure are DNA strand breaks and chromosomal aberrations. It is reported that DNA is the principal target for the biologic effects of radiation, including cell killing, mutations, and carcinogenesis. Chromosomal aberrations are caused by double-strand DNA breaks when cells are irradiated with X-rays.

A) DNA strand breaks:

DNA single-strand breaks (SSBs) may occur when cells are irradiated with a modest dose of X-rays, which can be observed using DNA denaturation. As far as cell killing is concerned, SSBs are of little biological consequence because they are repaired readily using the opposite strand as a template. If the repair is incorrect, it may result in a mutation. If the breaks are well separated when both of the DNA strands are broken, repair could also happen readily. However, when the breaks occur in both strands simultaneously or are separated by only a few base pairs, they may lead to a double-strand break (DSB). When double-strand breaks happen, a piece of chromatin snaps into two pieces. Doublestrand breaks are believed to be the most important lesions produced in chromosomes by radiation, resulting in cell killing, mutation, or carcinogenesis. DSBs can be measured using pulsed-field gel electrophoresis (PFGE) and the single-cell electrophoresis. DNA in cells is much more resistant to damage by radiation than free DNA because of the physical protection as well as the molecular repair reactions from the cell structure. It is also reported that DNA containing actively translating genes appears to be more sensitive to radiation. For a dose of 1~2 Gy, the number of DNA lesions per cell immediately after the exposure is approximately: base damage > 1000, singlestrand breaks ~ 1000, and double-strand breaks ~40.

B) Chromosomal aberrations:

When double-strand breaks are produced in the chromosomes as a consequence of incident X-rays, the resultant broken unpaired ends are sticky and can rejoin with other sticky ends (unpaired ends), causing chromosome aberrations and chromatid aberrations. Chromosomal aberrations in peripheral lymphocytes have been widely used as biomarkers of radiation exposure with the lowest detectable single dose of 0.25 Gy. The radiation dose can be estimated by comparison with in vitro cultures exposed to known doses and used to determine whether the suspected exposure to a person is a real exposure.

2.2.2 Radiation Exposure Effects on Cellular Level

The radiation-induced damage on DNA in the cell nucleus is responsible for most of the radiation-induced cell death. Different types of cells have various levels of sensitivity to radiation. In 1906, radiologist Jean Bergonie and histologist Louis Tribondeau put forward the Law of Bergonie and Tribondeau stating:

1) Stem or immature cells are more radiosensitive than mature cells;

2) Younger tissues and organs are more radiosensitive than older tissues and organs;

3) The higher the metabolic cell activity, the more radiosensitive it is;

4) The greater the proliferation and growth rate for tissues, the greater the radiosensitivity;

Cell survival curves are used to describe the relationship between the radiation dose and the proportion of cells that survive. In general, a dose of 100 Gy is necessary to destroy cell function in non-proliferating systems, while the mean lethal dose for loss of proliferative capacity is usually less than 2 Gy.

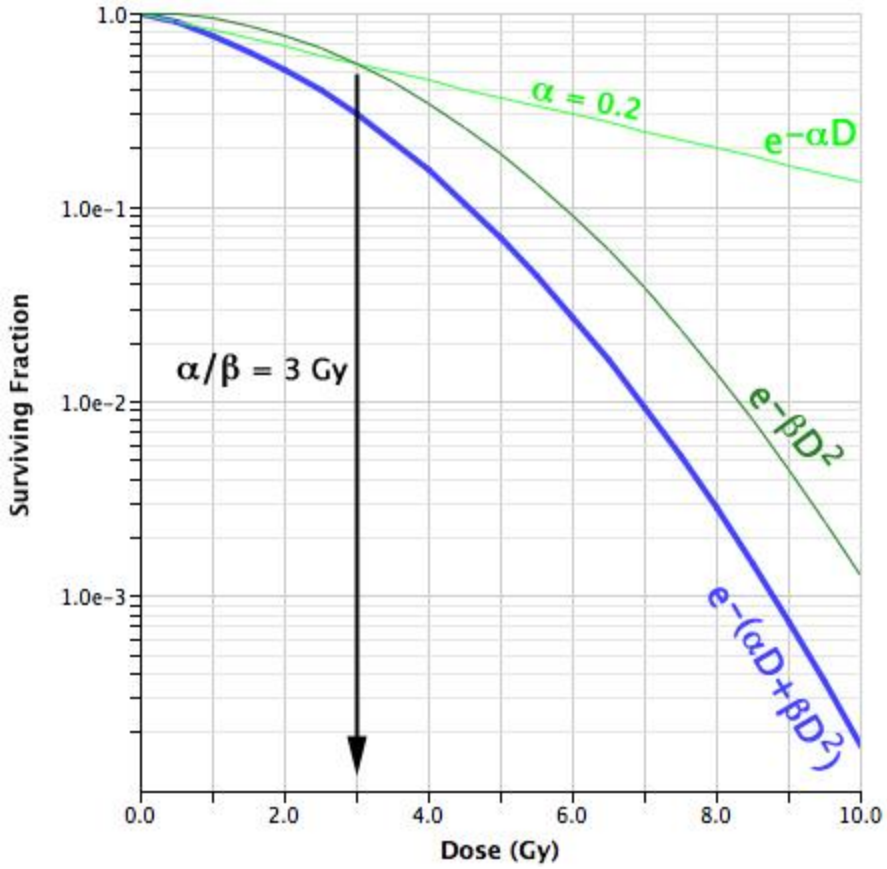

Fig: 2.5 A survival curve using the standard LQ formula $e^{-(\alpha D+\beta D2)}$ where $\alpha = 0.2$ and $\alpha/\beta = 3$. The components of cell killing are equal where the curves $e^{-\alpha D}$ and $e^{-\beta D2}$ intersect. This occurs at dose $D = \alpha/\beta$ (3 Gy in this example).

2.2.3 High-dose Effects and Low-dose Effects

High-dose radiation exceeding the threshold dose could result in deterministic effects, including skin damage, cataractogenesis, sterility, and even death. The practical threshold dose in diagnostic radiology is 2 Gy. As a quantitative description of irradiation effects, the half lethal dose (LD50) is defined as the uniform whole-body dose that would kill 50% of the population. The LD50 is 3 to 4 Gy within 60 days for young adults without medical intervention. Below the threshold for induction of deterministic effects (< 2 Gy), radiation can result in carcinogenesis, which is the principal concern in diagnostic radiology. It is a type of stochastic effect, with the severity of the effects independent of the radiation dose, but the probability of the cancer induction

increases with radiation dose. Radiationinduced carcinogenesis could be expressed using levels of radiation-induced risks.

2.2.4 Radiation-induced Risks

The biological consequence resulting from low-dose irradiation is often characterized by radiation-induced carcinogenic risks, because low-dose radiation acts principally on early stages of tumorigenesis based on available animal data. Studies of atomic bomb survivors, medical radiation, occupational radiation, and environmental radiation have been performed to estimate cancer risks. Epidemiological studies of the Japanese survivors of the Hiroshima and Nagasaki atomic bombs demonstrated a linear relationship between cancer incidence and organ dose over a range extending between two and three orders of magnitude. Major scientific bodies, including the Committee on the Biological Effects of Ionizing Radiation, International Committee on Radiological Protection, and the United Nations Scientific Committee on the Effects of Atomic Radiation all assume that radiation risks exist at low doses for radiation protection purposes. The linear no-threshold (LNT) model is by far the most popular model describing the relationship between radiation exposure and cancer development in humans.

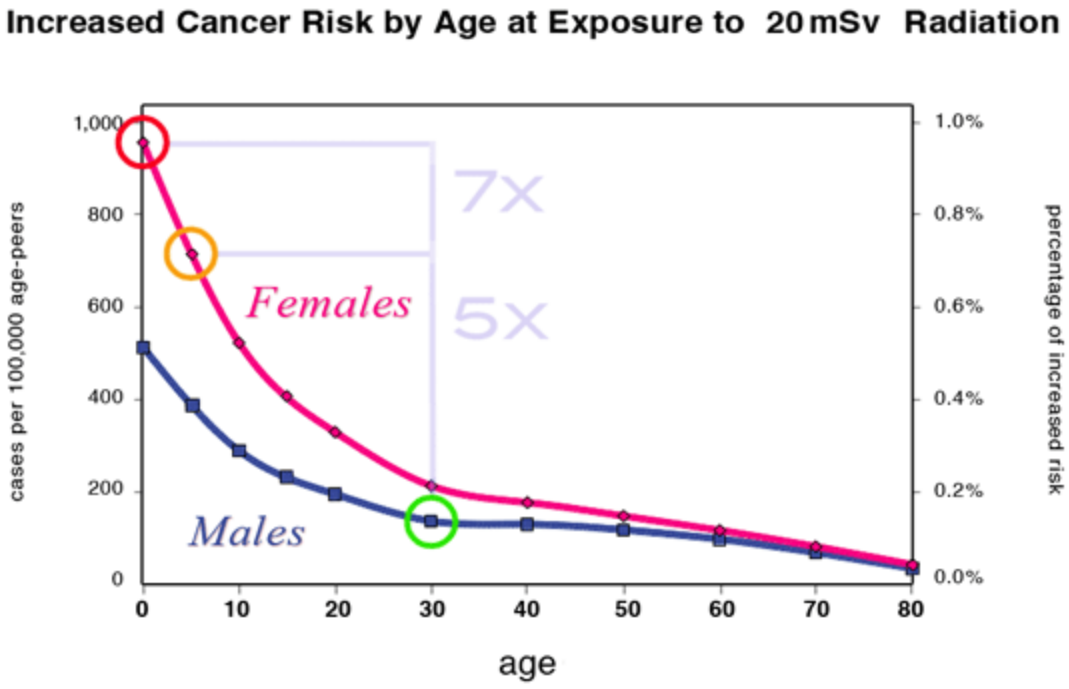

Figure 2.6: Increase cancer risk by age, BEIR VII Phase 2 Report

2.2.5 Effective Dose

The effective dose is a descriptor that can be used to characterize radiation exposure to patients in interventional radiology[33]. Computation of effective dose requires knowledge of absorbed dose to all irradiated organs and tissues, which may be obtained by means of Monte Carlo computational techniques or direct measurement in anthropomorphic phantoms[34]. Effective doses can be obtained from different measurement quantities, such as dose area product, or air kerma measurement.

In a study performed by Brambilla M et al[35], low mean effective dose estimates were shown to lie in extravascular procedures (4.8 - 28.2 mSv), intermediate effective dose values for neurointerventional procedures (12.6 - 32.9 mSv), and higher effective doses for vascular

procedures involving the abdomen (36.5 - 86.8 mSv). Calculations aiming at obtaining the DAP to effective dose conversion factor in abdominal and vascular interventional radiology showed a result of ~ 0.15 mSv/ Gy-cm 2

2.2.6 Energy imparted

Energy imparted in a patient during an IR procedure could also be used to calculate the effective dose, as advanced by Huda et al[36]. Under the condition of a uniform whole-body irradiation, the smaller mass results in a higher conversion factor to convert energy imparted to effective dose; under non-uniform exposure, the radiosensitivity of an irradiated region also needs to be taken into account when energy imparted is converted to effective dose[37]. Thus, an estimate of energy imparted on a patient undergoing any given radiology imaging procedure can be used to compute the effective dose and then converted to patient specific radiation-induced carcinogenesis risks[38].

2.4 Monte Carlo Applications.

2.4.1 Monte Carlo Radiation Transport Code

Monte Carlo N-Particle (MCNP)[39] is a general-purpose Monte Carlo code package that can be used for neutron, photon, electron, or coupled neutron/photon/electron transport. The MCNP system is maintained by a large group at Los Alamos National Laboratory and has many applications outside medical physics since it was originally a neutron–photon transport code used for reactor calculations. This code has a very powerful geometry package and has incorporated the electron transport part from the ETRAN code system. The great flexibility of this code makes it

run considerably slower than EGSnrc. Electron Gamma Shower (EGS) code was developed by Ralph Nelson et al in 1974. On the basis of this platform, the current EGSnrc system is developed as a package for Monte Carlo simulation of coupled electron-photon transport within the energy range of 1keV to 10 GeV[40]. EGSnrc improved its former version of EGS4 which was developed at Stanford Linear Accelerator Center (SLAC) and incorporated improvements in the implementation of the condensed history technique for the simulation of charged particle transport and better low energy cross sections. BEAMnrc, based on the EGSnrc code system, is a general purpose MC simulation system for modeling radiotherapy sources.

In order to simulate any particle interactions, MCNP solves the Boltzmann transport equation, defined as:

$$\Psi(\vec{r},\vec{v}) = \int \left(\int \Psi(\vec{r}',\vec{v}')\, C\left(\overrightarrow{v' \rightarrow \vec{v},\vec{r}}\right) d\overrightarrow{v'} + Q\left(\overrightarrow{r'},\vec{v}\right) \right) T(\vec{r}' \rightarrow \vec{r},\vec{v})\, d\vec{r} \qquad (12)$$

The $\Psi(\vec{r},\vec{v})$ term defines the collision density of particles across the whole simulation space. The C is called the collision kernel, which accounts for particles changing their velocity at a given location. The T term, on the other hand, is the transport kernel and accounts for the opposite case - a particle changing its location at a given velocity.

To give a bit more insight, let's take an example of the simulation of geometrically optimized flux reactor and in this simulations the Q term which is the source of the particle is defined as:

$$Q(r,v) = S(\vec{r},\vec{v}) + \int \Psi(\vec{r}',\vec{v}')\, F\left(\overrightarrow{v' \rightarrow \vec{v},\vec{r}}\right) \qquad (13)$$

S define the fact that the source is stationary, and that the primary particles will be emitted from a fixed point in the simulation space. The collision density term accounts for the fact that the core will be undergoing fission, define as F. What makes MCNP so powerful is the simultaneous use of the collision and transport kernels. Taking both factors into account

allows the simulation to look at particles that change velocity and direction at any point in the simulation space. Every interaction that a particle has with another particle is stored in the simulation memory. The states of the particles - energy, velocity, direction - are saved in order to extrapolate results and determine the convergence. The flow diagram in Figure 1, can also be seen in terms of particle histories, seen in Figure below.

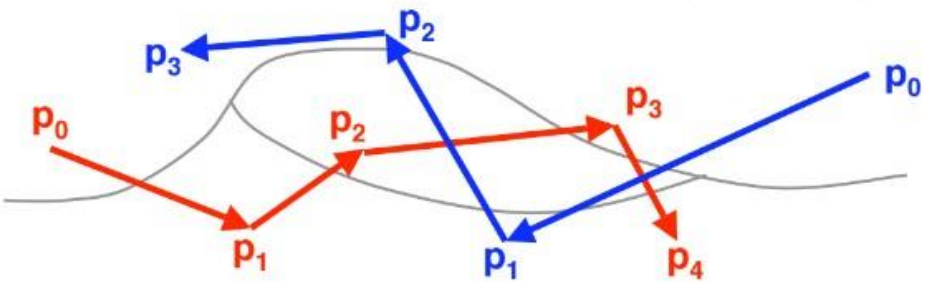

Figure 2.7: Particle interaction histories.

With the histories, MCNP is able to extrapolate where the particles will end up after future runs and what their energies will be. The final results are defined in the following way:

$$A = \int A(p)\Psi(p)dp \approx \frac{1}{M}\sum_{m=1}^{M}\left(\sum_{k=1}^{\infty}A(p_{k,m})\right) \qquad (14)$$

The final average state of the particle is the integral of the product between the collision density and the particle states. This integral can be estimated through a classic Riemann sum, where M is the number of particles and samples. The large value of M, the more accurate the final computed values are.

The PENELOPE code package has a detailed treatment of cross sections for lowenergy transport and a flexible geometry package which allows simulation of an accelerator[41]. The GEANT4 code is a general purpose code developed for particle physics applications[42], which can simulate the transport of many particle types (neutrons, protons, etc). GEANT4 has been used for various application in radiotherapy physics. It still demonstrates some problems when electron transport is involved and runs slower than EGSnrc in such applications, but overall the system is very powerful.

A) *Applications of MC software in Medical Physics and MCNP*

The Monte Carlo method could be used to perform calculations for radiation protection and dosimetry, radiation shielding, radiography, nuclear criticality safety, detector design and analysis, accelerator target design, and fission and fusion reactor design. In the medical physics area, the applications of Monte Carlo codes have been employed to conduct calculations on detection systems, imaging correction, absorbed doses, and radiation protection in nuclear medicine, diagnostic radiology and radiotherapy. They are also applied in treatment planning and brachytherapy in radiotherapy physics.

The MCNP input file describes the geometry of the problem, materials and radiation sources, and format and types of results needed from the calculation[43]. Specific problem geometries are developed by defining cells that are bounded by one or more surfaces. Cells can be filled with a specific material or defined as a void.

MCNP input files are structured into three major sections: cell cards, surface cards, and data cards. The cell card section is preceded by a one-line title card. In MCNP, the word “card” describes a

single line of input that can consist of up to 80 characters. A “section” consists of one or more cards:

Message Block +

blank line delimiter{optional}

One line problem title card

Cell cards[Block 1]

blank line delimiter

Surface cards[Block 2]

blank line delimiter

Data Cards [Block 3]

blank line terminator {optional}

Title Card

The title card is the first card in an MCNP input file. It can consist of up to 80 characters. It helps to describe the problem being modeled for future reference. In this way, the title card serves as a quick reference for the information contained in the input file and also a label for distinguishing between multiple input files. Also for future reference, the title will be echoed multiple times throughout the MCNP output file. After the title card, the first section is for the cell cards and has no blank line delimiter at the front of it. However, comment cards, describing the input deck for example, may be placed between the title card and the cell cards. Cells are used to define the shape and material content of the physical space of the problem. Date cards defines the type of particles, problem materials, radiation sources, how results are to be scored (or tallied), the level of detail for the physics of particle interactions, variance reduction techniques, cross section libraries, the

amount and type of output, and much more. In short, this third input block provides almost all problem specifications other than the geometry[44].

MCNP programs contain definitions for geometries in a 3D dimensional Cartesian coordinate system. A good way to look at cells, surfaces and their material denitions is the following. Let us suppose we have two surfaces A and B. Each surface has a negative and positive value, which is important for particle interactions. If a value is negative, then the surface is facing inwards relative to the origin.

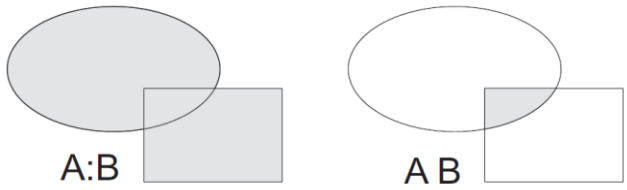

Figure 2.8: Example MCNP regions.

Surfaces can be combined to create cells. Defined as either unions or inter- sections, the resulting cells from surfaces A and B are seen in the above Figure. An important MCNP concept to remember is that three dimensional volumes can be created joining a series of two dimensional surfaces. For example, a cube is created as the intersection of six planes. Being able to identify which regions were required and which surfaces to ignore allowed us to carry out simulations more effectively and accurately.

MCNP also uses the SENSE concept defined for a point x', y', z' as having a +ve sense with respect to a Surface f (x, y, z) if f (x', y', z') > 0, and vice versa. A cell can be defined simply by the INTERSECTION operator (simply a blank space between two surface numbers on the cell card, provided that all points in the cell must have the same sense with respect to given bounding surfaces. Therefore, they can be no concave corners in a cell defined only by a intersections. The UNION operator, a colon (:), allows concave corners in cells and also cells that are completely disjoint. Spaces on either side of union operator are irrelevant. Intersection operations are performed first, followed by unions, but parentheses can be used to clarify operations or force a certain order. Note that intersection between two regions defines only points that belong to both regions at the same time, while a union defines all points that exist in both regions. For surfaces, say A and B, A - B defines a cell whose points have a +ve sense with respect to surface A and at the same time have a -ve sense wrt surface B; while -A: B defines everything in the universe with -ve sense wrt to A and a +ve sense wrt B. A cell may contain both operations, e.g. -AB(C: D) defines a cell in which the intersection of -A and B is intersected with the union of C and D.

The complement operator, #, stands for not in and is used to simplify cell specification; #n means that the current cell is the complement of cell n, while $(...) defines the complement ofthe portion of the cell description in the parentheses. The form # (n) is not allowed. Caution must be used with this operator as it can lead to some confusion, or an unnecessary increase in calculation of intersection of particle trajectory with surfaces. Repeated structure definitions are also allowed. Attention should be paid to the fact that a unique cell must be found for each particle position and that all points in the simulation space must exist within some cell. A dummy surface may be used to avoid ambiguity, also called ambiguity surface. The VOID card is useful in debugging geometry and calculating volume, however, that MCNP cannot detect overlapping cells or gaps between

cells until a particle track actually gets lost. The geometry-plotting feature of the code is always helpful to see the track of the simulation.

3. METHODS

3.1 Absorbed dose correction factor from Mono-Energetic Source

The dosimeter absorbed dose conversion factors (CFs) for LiF, Al_2O_3, and silicon were calculated using the MCNP6 [45] Monte Carlo radiation transport code (version 1.6). This code is a general-purpose radiation simulation program designed to transport and tally coupled neutrons, photons, and electrons through materials. Radiation transport was effected using the default MCPLIB04 photo-atomic cross section tables supplied with MCNP5; these tables are based on the EPDL97 data set [46].

The CF for each dosimeter type was obtained at depths between 0.2 and 10 cm in a simulated water phantom from a mono-energetic photon source. The photon source energies studied varied from 30 to 300 keV. Three irradiation geometries were investigated in this study. The first was an isotropic point source placed at the center of the water phantom, which is similar to an intra-cavity brachytherapy source irradiation geometry. The second geometry placed the point-source at the surface of the phantom to approximate an intra-operative brachytherapy geometry. Lastly, a 10 cm radial field was modeled to impinge normally on the phantom surface which approximated a diagnostic X-ray irradiation geometry. These comparisons to a brachytherapy source and diagnostic X-ray source specifically were chosen because such sources are among the most common generators of 30 to 300 keV photons.

The dosimeter calibration value for each photon energy studied was obtained for a LiF, Al_2O_3, and silicon dosimeter through the calculation of the dosimeter's CF in a non-scattering medium. These calibration values were calculated both theoretically (using Eq. 3) and through Monte Carlo simulations. For both techniques, the mass-energy absorption coefficient, μ_{en}/ρ, for water, LiF, and silicon was obtained by NIST [9] while the mass-energy absorption coefficient for Al_2O_3 was

calculated [47] as the mass-density weighted average of the constituent elemental absorption coefficients also published by NIST [9].

Monte Carlo calibration values were obtained using at least 1×10^8 photon histories for each photon energy analyzed to ensure that the relative uncertainty in the Monte Carlo output was less than 1%. In this study, a point-source was placed at the center of a 100 cm radial air phantom and the photon energy-fluence tallied at a distance of 20 cm using a 1 mm^3 tally volume. In this tally, the photon energy-fluence was obtained using the MCNP6 *FMESH tally. This tally then was coupled with a separate DE/DF card [45] which multiplied the energy-fluence by an appropriate mass energy absorption coefficient (e.g. Eq. 1) for water, LiF, Al_2O_3, and silicon which converted the photon energy fluence into the absorbed dose deposited to a CPE sized micro-phantom located at the site of the tally for each investigated material. From these results, the dosimeter calibration value (which is the CF obtained in a non-scattering medium) was calculated for each source photon energy as the ratio of the calculated absorbed dose to water divided by that obtained for the dosimeter as demonstrated in Eq. 3.

3.2 Phantom Simulation Parameters

An 80 x 80 x 80 cm water phantom was simulated for the geometry in which the point-source was located at the phantom center. Similarly, a 40 x 80 x 80 cm water phantom was simulated for both the surface point-source geometry and the 10 cm radial field geometry. These dimensions were chosen to obtain the maximum photon scatter contributions [10] to absorbed dose for the photon energies studied. For these phantom studies, a total of 1×10^9 photon histories were modeled to obtain a relative uncertainty in the MCNP tally less than 1% and the photon energy fluence tallied

at depths (that is, distances from the source) between 0.2 and 30 cm using a series of $1mm^3$ cubic mesh-volumes. Similar to the procedure described above, energy-fluence was tallied using the *FMESH tally and absorbed dose calculated using the appropriate DE/DF cards for each material of interest. It should be noted that the MCNP6 code has more direct methods of obtaining an absorbed dose, yet this approach is advantageous for this geometry because water is the only material in which photons are transported [48]. Therefore, in these simulations, the absorbed dose calculations will not be perturbed by non-water equivalent materials located upstream from the tally point. Also, because these calculations require CPE, data were not obtained at depths less than 2 mm. This depth was based on the 1.77 mm maximum range achievable in water for 500 keV photo-electrons [49]. Again, using the absorbed doses deposited at a specified depth for each material, the dosimeter CFs were calculated as the ratio of absorbed dose to water (D_{H2O}) to that of the dosimeter ($D_{dosimeter}$).

3.3 Absorbed dose correction factor for Poly-Energetic Sources Yb-169 and Ir-192

Radiation transport calculations were performed on a Windows-based personal computer running the MCNP6 Monte Carlo computer code. The Yb-169 and Iridium-192 photons spectra used for this simulations were obtained from the Lawrence Berkeley National Laboratory website[50]. Simulated photons transport through the water phantom with photon and secondary electron transport replicated using default MCPLIB04 photoatomic cross-sectional tables supplied with MCNP6. Simulations were performed for water phantom with a total of 1×10^9 photon history for each simulation. All simulations were performed in the photon and electron transport mode (Mode: p,e in the MCNP code) so that both primary photons and resulting secondary electrons were properly transported[51] . The complete Iridium-192 photon spectrum, presented by Firestone and

Ekström[50], was used in these calculations and the total uncertainty in the spectrum, $\sigma I\gamma$ relative = 0.5%, calculated as an intensity-weighted average of the uncertainty in each spectral line also presented by Firestone and Ekström[52]. Sufficient source photon histories were processed for each analysis to obtain a relative uncertainty in the MCNP tally convergence of less than 3% in any Yb-169 and Ir-192 spectral energy line. The low yield photons in the Yb and Ir isotopes will be the limiting factor in this convergence, higher yield photons will have much lower uncertainities and resulted in an overall tally convergence uncertainty of approximately 0.1% in the volume of interest.

The quantification of the spectral self absorption for Yb and Ir isotopes was not required because of the point source geometry. The point source was placed in the center of an evacuated environment and the energy spectrum emergent from the cource scored with the MCNP F04 tally ($1/cm^2$/KeV/S.P.) in keV increment photon energy bins for both of the isotopes. The intensity weighted average energy was calculated from these data as,

$$\bar{E} = \frac{\sum_{i=1}^{n} E_i \, \varphi_i}{\sum_{i=1}^{n} \varphi_i} \tag{11}$$

Where φ_i is the flux talley calculated by MCNP at energy E_i for all the energy bins.

The Yb-169 and Ir-192 sources were simulated as a point source and the absorbed dose deposited in three dosimeters was analyzed at phantom depths of 1 to 34 cm at each cm. Absorbed dose to three dosimeters were calculated using MCNP6 *F04 energy-fluence tally coupled with DE/DF dose conversion factor cards. These dose conversion cards multiplied the energy fluence tally by the appropriate mass absorption coefficient for all the dosimeter under study to obtain the calculated dose at the tallied depth for both LiF and water. This method allows the dose calculation without perturbing from the outside region of the phantom. Tally volumes are created to reduce

volumetric averaging effects to below 3%. The resulting MCNP tally output at each tally location for all there dosimeters were multiplied by the Yb and Ir conversion factor to convert the output into the the more familiar units of cGy/hr* mCi[53].

4. RESULTS AND DISCUSSION

4.1 Point source at cavity center

The absorbed dose conversion factors obtained from source-photons emitted with energies between 30 and 300 keV are presented in Table 1 for LiF dosimeters, Table 2 for Al_2O_3 dosimeters, and Table 3 for silicon dosimeters. These data are presented at depths between 0.2 cm and 10 cm for a point source geometry with the source located at phantom center. In these and all other tables, the MCNP reported (in-air) dosimeter calibration values also are presented for reference. It should be noted that, on average, these calibration values agree with their theoretical calculated counterpart (obtained using Eq. 3) to within 1%; no deviation in these data was greater than 4%. Therefore, to best correlate with the MCNP derived CFs, the MCNP reported calibration values are presented in place of the theoretically computed calibration values.

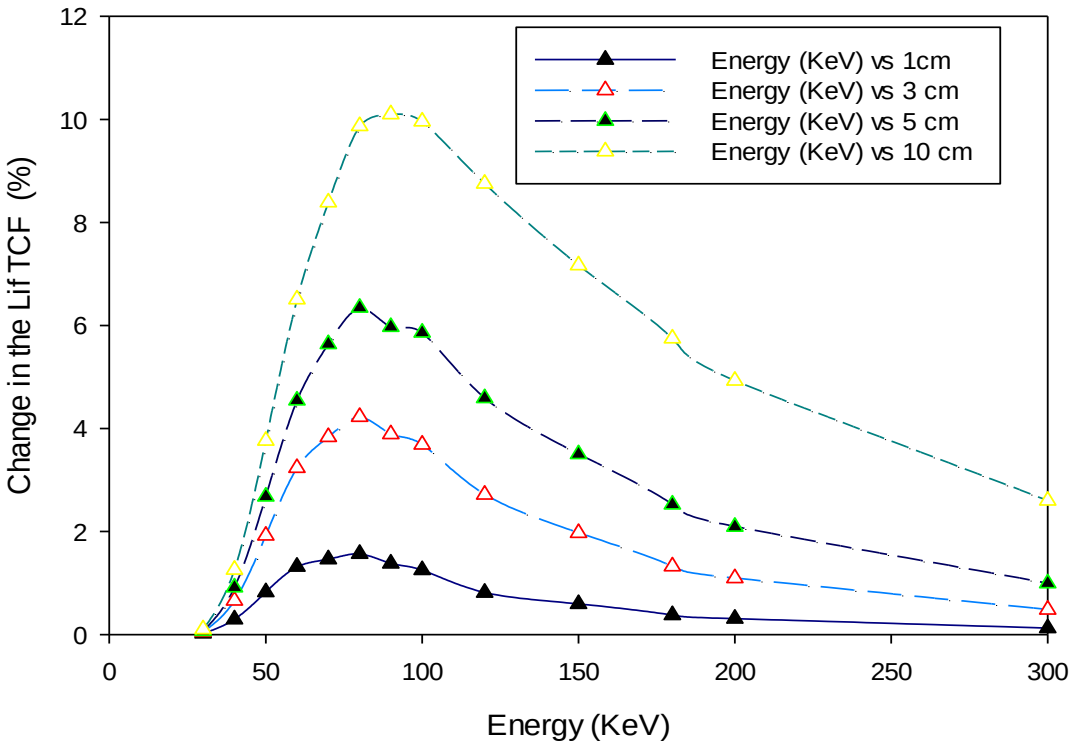

Figure 4.1: LiF percent deviation of the dosimeter's CF relative to an in-air calibration value for at distances of 1 cm, 3 cm, 5 cm, and 10 cm in a water phantom. These dosimetric values represent the response from a monoenergetic point-source located at the center of a pseudo-infinite water phantom. In this figure, the author selected 5% significant deviation level is depicted as a horizontal dashed line.

The CF values for LiF (Table 1) were found to have a minimum value of 0.852 for a 30 keV source at a 10 cm depth and a maximum value of 1.198 for a 300 keV source at a 2 mm depth a 41% variation. The minimum Al_2O_3 CF value was 0.285 and the maximum was 1.120 a 293% intrinsic variation, while silicon had a minimum CF value of 0.134 and a maximum of 1.083 a 708% intrinsic variation. Perhaps more importantly, the deviation between each CF value and that dosimeter's calibration value was calculated and is presented in Fig. 2 at depths of 1, 3, 5, 7, and 10 cm. For these data, the deviations exceed the author's selected 5% significance limit for both the Al_2O_3 and silicon dosimeters at each depth. This deviation increases as a function of phantom

depth such that an Al_2O_3 dosimeter was found to achieve a maximum 43% deviation at a depth of 10 cm for 100 keV photons while a silicon dosimeter achieved a 61% deviation at a depth of 10 cm for 150 keV photons. The LiF dosimeter, on the other hand, reached a significant deviation (> 5%) from its calibration value only at depths of 7 cm or greater; this is expected due to the reasonably equivalent electron density [Z_{eff} (LiF) = 8.3] between LiF and water [Z_{eff} (H_2O) = 7.5]. For each dosimeter, the maximum deviation from its calibration value for this analysis geometry was 9% for LiF (10 cm depth, 100 keV), 43% for Al_2O_3 (10 cm, 100 keV), and 61% for silicon (10 cm, 150 keV). Because Fig. 2 demonstrates an increased deviation with depth, measurements taken at depths greater than 10 cm require additional analysis

Table 4.1: Absorbed dose CF values for LiF dosimeters from monoenergetic photons emitted from a point-source located at phantom center.

Energy	Cal.	Depth (cm)											
(keV)	value	0.2	0.5	1	2	3	4	5	6	7	8	9	10
30	0.852	0.853	0.852	0.852	0.852	0.852	0.852	0.852	0.852	0.852	0.852	0.852	0.852
40	0.876	0.879	0.878	0.876	0.873	0.871	0.870	0.869	0.868	0.868	0.867	0.867	0.867
50	0.914	0.927	0.922	0.916	0.908	0.903	0.899	0.895	0.893	0.891	0.890	0.888	0.887
60	0.961	0.985	0.977	0.967	0.952	0.941	0.933	0.927	0.923	0.918	0.916	0.913	0.910
70	1.005	1.036	1.028	1.015	0.995	0.981	0.969	0.961	0.953	0.947	0.942	0.938	0.935
80	1.046	1.083	1.074	1.060	1.036	1.018	1.003	0.992	0.983	0.975	0.968	0.964	0.958
90	1.075	1.112	1.104	1.091	1.067	1.048	1.032	1.020	1.009	1.000	0.992	0.985	0.979
100	1.102	1.138	1.130	1.118	1.095	1.075	1.058	1.044	1.032	1.023	1.014	1.006	0.999
120	1.130	1.159	1.154	1.145	1.127	1.110	1.094	1.080	1.068	1.057	1.048	1.039	1.033
150	1.162	1.183	1.180	1.174	1.160	1.145	1.131	1.119	1.107	1.096	1.085	1.077	1.069
180	1.175	1.190	1.188	1.184	1.173	1.163	1.151	1.141	1.130	1.121	1.112	1.103	1.094
200	1.18	1.194	1.192	1.188	1.180	1.171	1.161	1.151	1.141	1.133	1.124	1.117	1.108
300	1.192	1.198	1.198	1.196	1.192	1.187	1.182	1.176	1.170	1.164	1.158	1.152	1.145

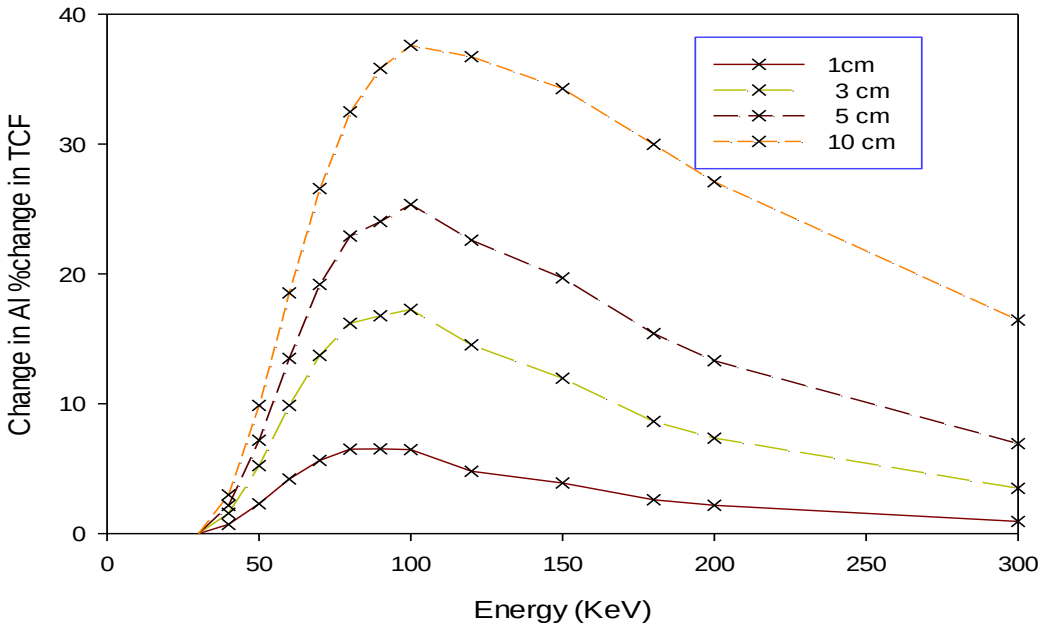

Figure 4.2: LiF percent deviation of the dosimeter's CF relative to an in-air calibration value at 1 cm, 3 cm, 5 cm, and 10 cm depths in a water phantom for a point-source located at the surface of a pseudo-infinite water phantom. In this figure, the author selected 5% significant in deviation level is depicted as a horizontal dashed line

Table 4.2: Absorbed dose CF values Al_2O_3 dosimeters from a point-source located at the center of a water phantom..

Energy	Cal.	Depth (cm)											
(keV)	value	0.2	0.5	1	2	3	4	5	6	7	8	9	10
30	0.285	0.285	0.285	0.285	0.285	0.285	0.285	0.285	0.285	0.285	0.285	0.286	0.285
40	0.306	0.306	0.305	0.304	0.301	0.300	0.299	0.298	0.298	0.297	0.297	0.296	0.296
50	0.353	0.354	0.349	0.343	0.334	0.329	0.325	0.322	0.320	0.318	0.317	0.315	0.314
60	0.426	0.428	0.418	0.404	0.384	0.371	0.362	0.356	0.351	0.346	0.343	0.340	0.338
70	0.519	0.522	0.506	0.483	0.449	0.426	0.409	0.398	0.388	0.381	0.375	0.369	0.366
80	0.616	0.621	0.599	0.566	0.517	0.484	0.459	0.442	0.428	0.417	0.407	0.401	0.394
90	0.704	0.710	0.685	0.647	0.587	0.545	0.513	0.491	0.470	0.456	0.443	0.433	0.424
100	0.793	0.799	0.772	0.729	0.657	0.605	0.567	0.537	0.513	0.495	0.480	0.465	0.454
120	0.889	0.895	0.873	0.834	0.763	0.705	0.658	0.618	0.590	0.564	0.545	0.526	0.514
150	1.018	1.022	1.003	0.968	0.898	0.833	0.778	0.733	0.696	0.664	0.634	0.613	0.592
180	1.06	1.063	1.050	1.024	0.967	0.913	0.861	0.815	0.775	0.742	0.711	0.683	0.658
200	1.084	1.087	1.076	1.054	1.003	0.953	0.903	0.858	0.819	0.785	0.753	0.728	0.700
300	1.119	1.120	1.115	1.105	1.079	1.049	1.016	0.982	0.952	0.920	0.892	0.864	0.833

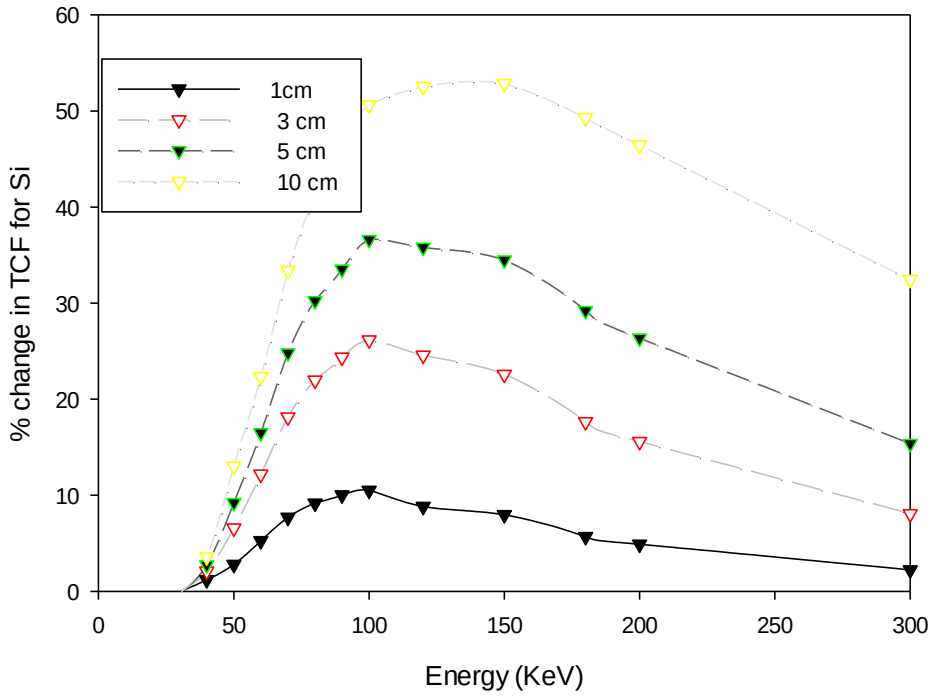

Figure 4.3: Si percent deviation of the dosimeter's CF relative to an in-air calibration value at 1 cm, 3 cm, 5 cm, and 10 cm depths in a water phantom for a point-source located at the surface of a pseudo-infinite water phantom. In this figure, the author selected 5% significant in deviation level is depicted as a horizontal dashed line.

Table 4.3: Absorbed dose CF values for silicon dosimeters from a point-source located at the center of a water phantom.

Energy	Cal.	Depth (cm)											
(keV)	value	0.2	0.5	1	2	3	4	5	6	7	8	9	10
30	0.134	0.134	0.134	0.134	0.134	0.134	0.134	0.134	0.134	0.134	0.134	0.134	0.134
40	0.145	0.145	0.144	0.143	0.142	0.141	0.141	0.141	0.140	0.140	0.140	0.140	0.140
50	0.171	0.172	0.169	0.165	0.161	0.158	0.155	0.154	0.153	0.151	0.151	0.150	0.149
60	0.216	0.218	0.211	0.202	0.190	0.182	0.177	0.173	0.170	0.167	0.166	0.164	0.163
70	0.283	0.286	0.274	0.257	0.233	0.217	0.207	0.199	0.193	0.189	0.185	0.181	0.180
80	0.359	0.363	0.345	0.318	0.280	0.257	0.240	0.228	0.219	0.212	0.205	0.202	0.197
90	0.444	0.450	0.425	0.389	0.337	0.303	0.278	0.262	0.247	0.238	0.229	0.222	0.216
100	0.536	0.544	0.512	0.466	0.397	0.351	0.319	0.296	0.278	0.265	0.254	0.244	0.236
120	0.668	0.675	0.644	0.593	0.507	0.445	0.399	0.364	0.340	0.318	0.303	0.288	0.279
150	0.868	0.875	0.841	0.781	0.674	0.588	0.522	0.473	0.435	0.405	0.377	0.359	0.341
180	0.952	0.958	0.931	0.881	0.782	0.697	0.624	0.566	0.519	0.482	0.450	0.423	0.399
200	1.002	1.008	0.984	0.939	0.843	0.759	0.683	0.621	0.571	0.530	0.494	0.467	0.439
300	1.081	1.083	1.072	1.049	0.992	0.930	0.867	0.807	0.757	0.707	0.667	0.628	0.589

4.2 Surface point source geometry

The dosimeter CF values for a surface point-source geometry are presented in Tables 4, 5, and 6 respectively for LiF, Al_2O_3, and silicon. In each table, the MCNP obtained dosimeter calibration values also are provided for each dosimeter type. Here, the CF values for LiF vary between 0.852 and 1.192 (40% increase). Similarly, the Al_2O_3 CF values increased from 0.285 to 1.116 (292%), and the silicon CF values increased from 0.134 to 1.076 (703%). These maximum values were slightly lower than that obtained in the previous section which could indicate a slightly lower absorbed dose contribution from scattered photons. Figure 4.3 presents the deviation between these data and the dosimeter's calibration value at measurement depths of 1, 3, 5, 7, and 10 cm. Again, both Al_2O_3 and silicon exceed the significant deviation of 5% for nearly all measurement depths and source photon energies while the LiF dosimeter remained under this level except for photon energies between roughly 80 keV to 120 keV and only at a 10 cm depth. In this figure, the maximum deviation was found to be 6% for LiF (10 cm, 100 keV), 38% for Al_2O_3 (10 cm, 100 keV), and 53% for silicon (10 cm, 150 keV).

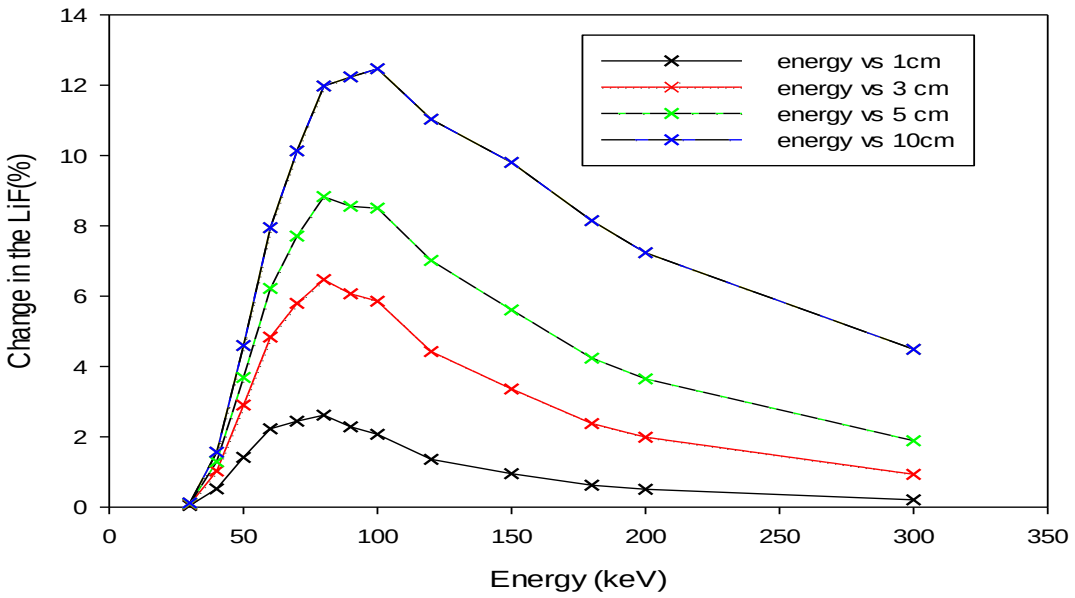

Figure 4.4: LiF percent deviation of the dosimeter's CF relative to an in-air calibration value at 1 cm, 3 cm, 5 cm, and 10 cm depths in a water phantom for a point-source located at the surface of a pseudo-infinite water phantom.

Table4.4: Absorbed dose CF values for LiF dosimeters from monoenergetic photons emitted from a point-source located at phantom surface.

Energy	Cal.	Depth (cm)											
(keV)	value	0.2	0.5	1	2	3	4	5	6	7	8	9	10
30	0.852	0.852	0.852	0.852	0.852	0.852	0.852	0.852	0.852	0.852	0.852	0.852	0.852
40	0.876	0.875	0.875	0.874	0.873	0.872	0.872	0.871	0.871	0.871	0.870	0.870	0.870
50	0.914	0.912	0.911	0.909	0.905	0.904	0.902	0.901	0.900	0.898	0.898	0.897	0.897
60	0.961	0.958	0.955	0.951	0.946	0.943	0.939	0.937	0.934	0.931	0.930	0.929	0.928
70	1.005	1.002	0.998	0.994	0.986	0.981	0.976	0.973	0.969	0.966	0.963	0.961	0.958
80	1.046	1.041	1.037	1.031	1.023	1.016	1.011	1.005	1.003	0.999	0.995	0.993	0.989
90	1.075	1.071	1.066	1.062	1.052	1.045	1.040	1.034	1.030	1.027	1.020	1.019	1.017
100	1.102	1.099	1.094	1.087	1.079	1.071	1.065	1.060	1.056	1.051	1.048	1.044	1.040
120	1.13	1.128	1.125	1.120	1.112	1.106	1.101	1.096	1.091	1.087	1.083	1.079	1.075
150	1.162	1.160	1.157	1.153	1.146	1.141	1.136	1.132	1.128	1.122	1.121	1.117	1.114
180	1.175	1.173	1.171	1.168	1.162	1.159	1.155	1.151	1.148	1.145	1.142	1.138	1.137
200	1.18	1.179	1.177	1.174	1.171	1.168	1.164	1.160	1.159	1.155	1.153	1.150	1.148
300	1.192	1.192	1.191	1.189	1.187	1.185	1.184	1.182	1.180	1.178	1.177	1.176	1.174

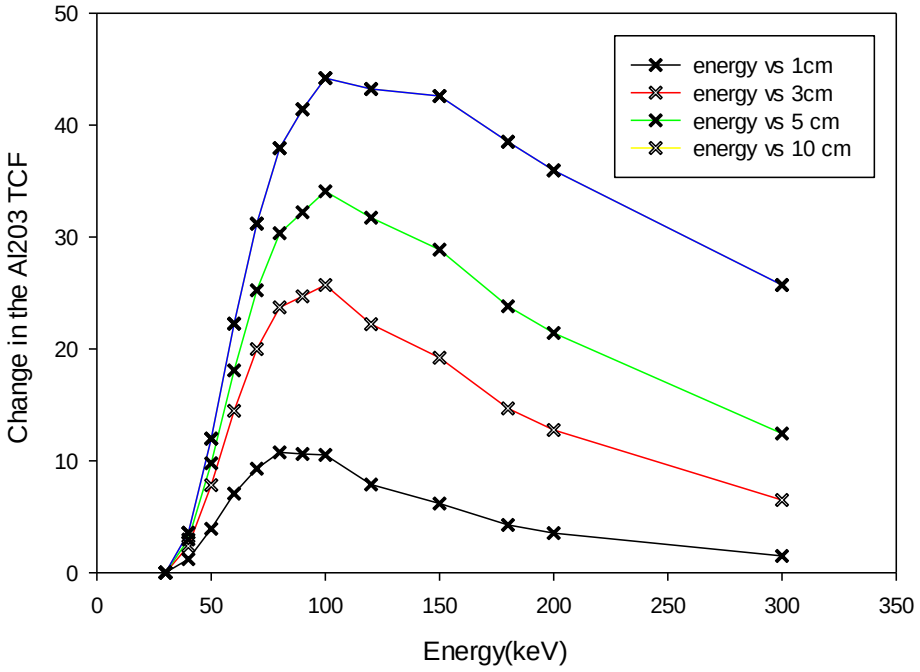

Figure 4.5: Al percent deviation of the dosimeter's CF relative to an in-air calibration value at 1 cm, 3 cm, 5 cm, and 10 cm depths in a water phantom for a point-source located at the surface of a pseudo-infinite water phantom. In this figure, the authors' selected 5% significant in deviation level is depicted as a horizontal dashed line.

Table 4.5: Absorbed dose CF values for Al_2O_3 dosimeters from a point-source located at the surface of a water phantom.

Energy	Cal.	Depth (cm)											
(keV)	value	0.2	0.5	1	2	3	4	5	6	7	8	9	10
30	0.285	0.285	0.285	0.285	0.285	0.285	0.285	0.285	0.285	0.285	0.285	0.285	0.285
40	0.306	0.306	0.305	0.304	0.303	0.302	0.300	0.300	0.299	0.298	0.298	0.298	0.297
50	0.353	0.351	0.348	0.345	0.339	0.334	0.331	0.328	0.326	0.323	0.321	0.320	0.318
60	0.426	0.421	0.416	0.408	0.394	0.384	0.376	0.368	0.363	0.357	0.353	0.350	0.347
70	0.519	0.511	0.503	0.489	0.466	0.447	0.432	0.419	0.410	0.400	0.393	0.387	0.381
80	0.616	0.607	0.594	0.576	0.542	0.517	0.494	0.475	0.459	0.446	0.434	0.426	0.416
90	0.704	0.694	0.680	0.658	0.619	0.586	0.557	0.535	0.512	0.495	0.479	0.467	0.452
100	0.793	0.781	0.766	0.742	0.697	0.656	0.621	0.592	0.566	0.543	0.524	0.509	0.495
120	0.889	0.880	0.868	0.847	0.803	0.760	0.723	0.688	0.658	0.630	0.608	0.585	0.563
150	1.018	1.009	0.998	0.979	0.937	0.896	0.854	0.818	0.779	0.748	0.716	0.691	0.669
180	1.06	1.054	1.047	1.033	1.002	0.969	0.931	0.897	0.861	0.831	0.802	0.773	0.742
200	1.084	1.079	1.073	1.061	1.034	1.005	0.969	0.940	0.907	0.876	0.844	0.818	0.791
300	1.119	1.116	1.114	1.108	1.095	1.080	1.062	1.041	1.018	0.993	0.973	0.948	0.935

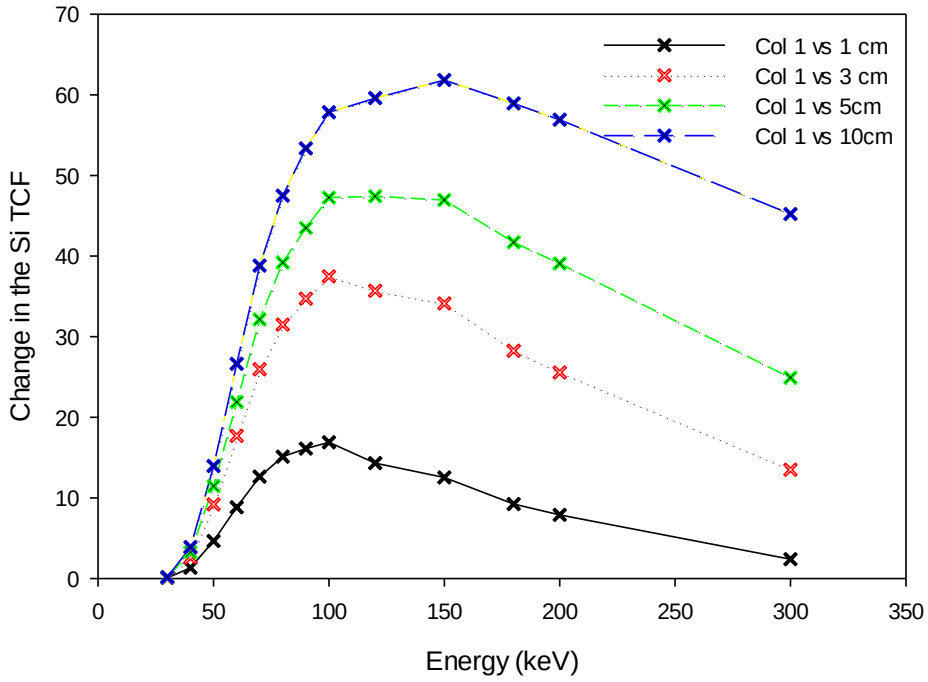

Figure 4.6: Al percent deviation of the dosimeter's CF relative to an in-air calibration value at 1 cm, 3 cm, 5 cm, and 10 cm depths in a water phantom for a point-source located at the surface of a pseudo-infinite water phantom. In this figure, the authors' selected 5% significant in deviation level is depicted as a horizontal dashed line.

Table 4.6: Absorbed dose CF values for silicon dosimeters from a point-source located at the surface of a water phantom.

Energy	Cal.	Depth (cm)											
(keV)	value	0.2	0.5	1	2	3	4	5	6	7	8	9	10
30	0.134	0.134	0.134	0.134	0.134	0.134	0.134	0.134	0.134	0.134	0.134	0.134	0.134
40	0.145	0.144	0.144	0.144	0.143	0.142	0.142	0.141	0.141	0.141	0.140	0.140	0.140
50	0.171	0.170	0.169	0.167	0.163	0.161	0.159	0.157	0.156	0.154	0.153	0.153	0.151
60	0.216	0.213	0.210	0.205	0.196	0.190	0.185	0.181	0.177	0.174	0.171	0.170	0.168
70	0.283	0.278	0.271	0.262	0.245	0.232	0.222	0.213	0.207	0.200	0.196	0.193	0.189
80	0.359	0.351	0.341	0.326	0.300	0.280	0.264	0.250	0.240	0.230	0.223	0.217	0.211
90	0.444	0.433	0.420	0.399	0.364	0.336	0.312	0.295	0.277	0.265	0.254	0.245	0.235
100	0.536	0.523	0.506	0.480	0.434	0.396	0.365	0.340	0.319	0.301	0.286	0.275	0.265
120	0.668	0.654	0.637	0.609	0.553	0.504	0.463	0.429	0.399	0.374	0.355	0.335	0.317
150	0.868	0.852	0.833	0.799	0.732	0.672	0.615	0.569	0.523	0.489	0.455	0.430	0.409
180	0.952	0.940	0.925	0.898	0.841	0.784	0.724	0.674	0.625	0.586	0.550	0.516	0.483
200	1.002	0.992	0.978	0.953	0.900	0.846	0.785	0.738	0.689	0.644	0.602	0.569	0.537
300	1.081	1.076	1.070	1.057	1.027	0.994	0.956	0.915	0.870	0.825	0.792	0.750	0.730

4.3 Field source result.

Lastly, the dosimeter in-air calibration values and in-phantom CF values are presented in Tables 7, 8, and 9 for a 10 cm radial field impinging on the phantom surface. While the minimum CF value for each dosimeter was found to remain relatively unchanged from previous irradiation geometries, the maximum value for LiF was calculated to be 1.198, Al_2O_3 to be 1.075, and silicon to be 0.983. Presents the percent deviation between these data and the dosimeter's calibration value; again, Al_2O_3 and silicon exceed the significant deviation of 5% for nearly all measurement depths and source photon energies while the LiF dosimeter remained under this level except for photon energies between roughly 60 to 160 keV and at a depth of 10 cm. In this figure, the maximum deviation was found to be 7% for LiF (10 cm, 90 and 100 keV), 34% for Al_2O_3 (10 cm, 100 keV), and 47% for silicon (10 cm, 150 keV). In this study, the field was modeled to have a radius of 10 cm. The results are within 3 % for LiF, within 13% for Al and within 24% for Si.

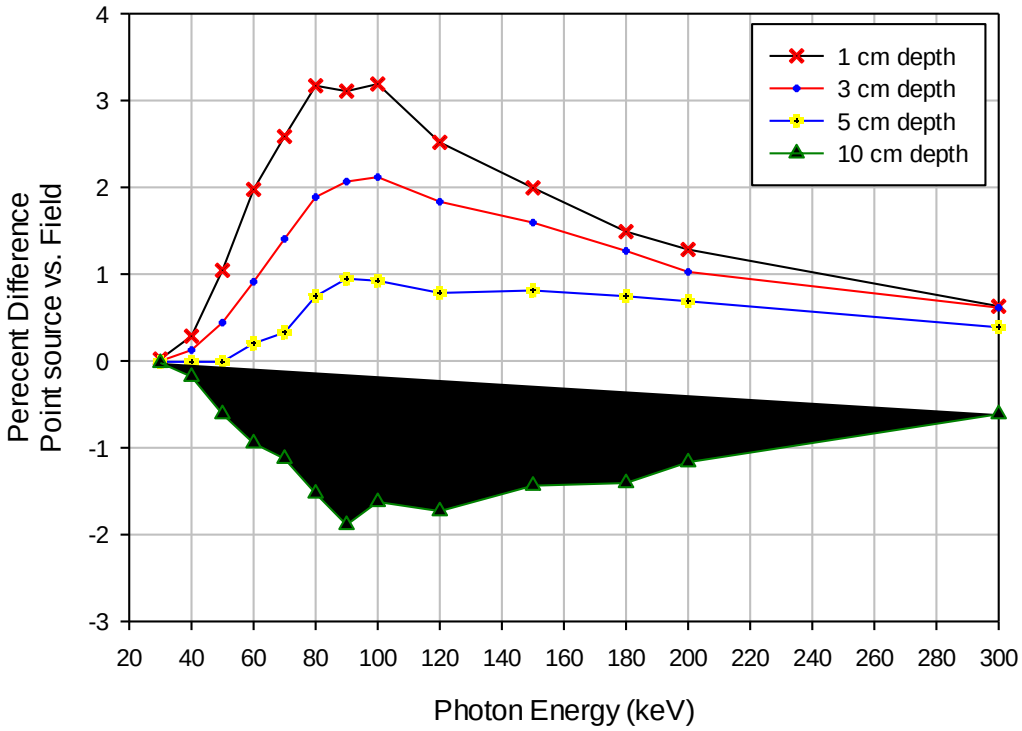

Figure 4.7: LiF percent deviation in CF form point source vs Field source impinging normally on the surface of the water phantom. In this study, the field was modeled to have a radius of 10 cm. The results are within 3 %.

Table 4.7: Absorbed dose CF values for LiF dosimeters from monoenergetic photons emitted from a 10 cm radial field.

Energy	Cal.	Depth (cm)											
(keV)	value	0.2	0.5	1	2	3	4	5	6	7	8	9	10
30	0.852	0.853	0.852	0.852	0.852	0.852	0.852	0.852	0.852	0.852	0.852	0.852	0.852
40	0.876	0.879	0.878	0.876	0.875	0.873	0.872	0.871	0.870	0.869	0.869	0.868	0.868
50	0.914	0.925	0.922	0.918	0.913	0.908	0.905	0.901	0.899	0.896	0.894	0.893	0.891
60	0.961	0.981	0.976	0.970	0.960	0.951	0.945	0.938	0.933	0.929	0.924	0.923	0.919
70	1.005	1.032	1.026	1.019	1.006	0.995	0.985	0.976	0.969	0.962	0.957	0.953	0.948
80	1.046	1.079	1.072	1.064	1.048	1.035	1.023	1.012	1.003	0.994	0.987	0.981	0.974
90	1.075	1.108	1.102	1.095	1.080	1.067	1.054	1.044	1.032	1.023	1.014	1.007	0.998
100	1.102	1.134	1.129	1.122	1.108	1.094	1.081	1.069	1.058	1.048	1.038	1.030	1.023
120	1.13	1.156	1.153	1.148	1.137	1.126	1.115	1.104	1.094	1.084	1.076	1.066	1.056
150	1.162	1.182	1.179	1.176	1.168	1.159	1.150	1.141	1.131	1.123	1.113	1.105	1.098
180	1.175	1.189	1.187	1.185	1.180	1.174	1.166	1.159	1.152	1.145	1.137	1.130	1.121
200	1.18	1.193	1.191	1.189	1.185	1.180	1.174	1.168	1.162	1.155	1.147	1.141	1.134
300	1.192	1.198	1.198	1.197	1.195	1.192	1.190	1.186	1.182	1.178	1.174	1.169	1.167

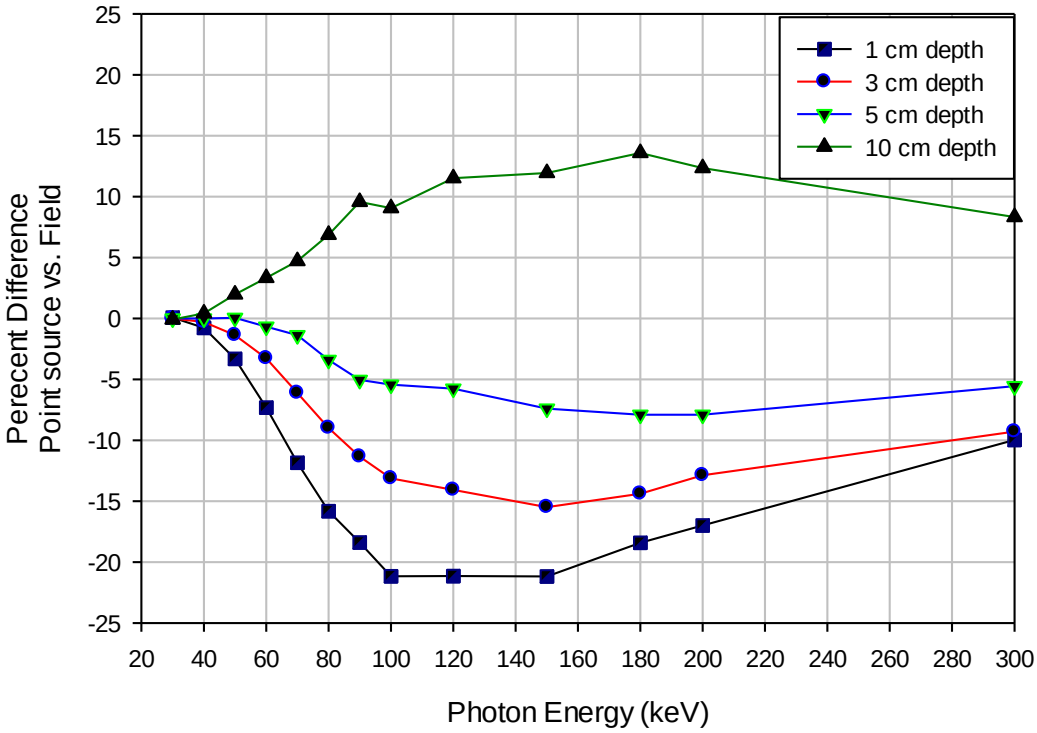

Figure 4.8: Al percent deviation in CF form point source vs Field source impinging normally on the surface of the water phantom. In this study, the field was modeled to have a radius of 10 cm. The results are within 13 %.

Table 4.8: Absorbed dose CF values for Al_2O_3 dosimeters from monoenergetic photons emitted from a 10 cm radial field.

Energy	Cal.	Depth (cm)											
(keV)	value	0.2	0.5	1	2	3	4	5	6	7	8	9	10
30	0.285	0.285	0.285	0.285	0.285	0.285	0.285	0.285	0.285	0.285	0.285	0.285	0.285
40	0.306	0.303	0.303	0.302	0.301	0.301	0.300	0.300	0.300	0.299	0.299	0.299	0.299
50	0.353	0.339	0.337	0.335	0.332	0.331	0.329	0.328	0.326	0.325	0.325	0.324	0.323
60	0.426	0.392	0.388	0.384	0.378	0.373	0.369	0.366	0.363	0.360	0.359	0.358	0.356
70	0.519	0.460	0.452	0.446	0.434	0.426	0.419	0.415	0.410	0.405	0.401	0.398	0.395
80	0.616	0.528	0.520	0.509	0.494	0.482	0.473	0.463	0.459	0.453	0.446	0.443	0.438
90	0.704	0.597	0.585	0.574	0.553	0.538	0.527	0.515	0.507	0.502	0.490	0.488	0.484
100	0.793	0.669	0.655	0.637	0.615	0.597	0.581	0.569	0.560	0.550	0.544	0.535	0.527
120	0.889	0.767	0.757	0.738	0.712	0.693	0.678	0.663	0.648	0.639	0.627	0.618	0.607
150	1.018	0.897	0.884	0.866	0.836	0.817	0.797	0.782	0.766	0.746	0.742	0.727	0.719
180	1.06	0.964	0.954	0.936	0.909	0.895	0.879	0.858	0.848	0.833	0.823	0.805	0.801
200	1.084	0.998	0.990	0.973	0.955	0.939	0.921	0.901	0.894	0.875	0.866	0.853	0.845
300	1.119	1.075	1.068	1.060	1.045	1.034	1.025	1.014	1.006	0.994	0.987	0.981	0.973

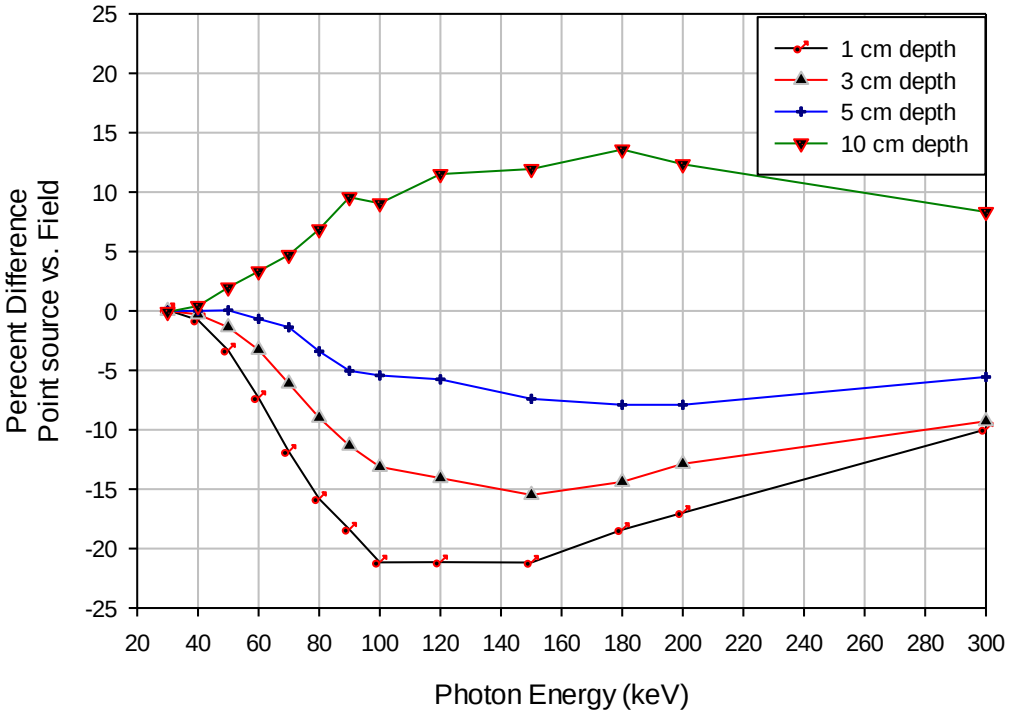

Figure 4.9: Al percent deviation in CF form point source vs Field source impinging normally on the surface of the water phantom. In this study, the field was modeled to have a radius of 10 cm. The results are within 24 %.

Table 4.9: Absorbed dose CF values for silicon dosimeters from monoenergetic photons emitted from a 10 cm radial field.

Energy	Cal.	Depth (cm)											
(keV)	value	0.2	0.5	1	2	3	4	5	6	7	8	9	10
30	0.134	0.134	0.134	0.134	0.134	0.134	0.134	0.134	0.134	0.134	0.134	0.134	0.134
40	0.145	0.143	0.143	0.143	0.142	0.142	0.142	0.141	0.141	0.141	0.141	0.141	0.141
50	0.171	0.163	0.162	0.161	0.159	0.158	0.157	0.157	0.156	0.155	0.155	0.155	0.154
60	0.216	0.195	0.193	0.190	0.186	0.184	0.181	0.179	0.177	0.176	0.175	0.174	0.174
70	0.283	0.240	0.235	0.231	0.223	0.218	0.213	0.210	0.207	0.204	0.201	0.200	0.198
80	0.359	0.289	0.283	0.274	0.264	0.255	0.249	0.242	0.240	0.235	0.231	0.228	0.225
90	0.444	0.345	0.335	0.326	0.309	0.298	0.289	0.280	0.274	0.270	0.261	0.260	0.257
100	0.536	0.408	0.395	0.378	0.359	0.344	0.331	0.321	0.314	0.306	0.302	0.295	0.289
120	0.668	0.511	0.500	0.480	0.452	0.433	0.418	0.404	0.390	0.382	0.371	0.363	0.353
150	0.868	0.673	0.654	0.630	0.592	0.568	0.544	0.527	0.508	0.487	0.483	0.467	0.458
180	0.952	0.777	0.760	0.733	0.692	0.671	0.648	0.621	0.607	0.588	0.575	0.554	0.549
200	1.002	0.834	0.821	0.791	0.762	0.737	0.709	0.680	0.669	0.643	0.632	0.614	0.603
300	1.081	0.983	0.968	0.952	0.922	0.901	0.884	0.864	0.849	0.826	0.815	0.805	0.791

4.4 Polyenergetic simulation result

The absorbed dose conversion factors obtained from source-photons emitted with energies between 30 and 1300 keV are calculated for LiF, Al_2O_3 and silicon dosimeters. In each table below, the MCNP obtained percentage change in dosimeter correction values as a function of depth of the phantom is shown for three dosimeter type. For easier comparision, these data also were graphed and are presented in figures. In each source simulations sufficient photon histories were performed to obtain a relative uncertainty in the tally convergence of less than 1%.

Table 4.10: Percentage change in correction factors for LiF dosimeters from monoenergetic photons emitted from a disk source located at phantom surface.

Energy			% change in calibration values		
(KeV)			Depth (cm)		
	1	4	8	17	34
30	0.01	0.14	0.21	0.00	0.00
50	1.54	3.98	4.72	5.85	6.61
80	2.50	9.40	12.77	13.48	15.6
100	1.95	9.17	13.41	15.46	16.4
120	1.43	7.80	12.24	15.15	16.5
150	1.06	6.40	11.1	14.88	16.0
180	0.49	4.59	9.19	13.23	14.8
200	0.37	4.00	8.35	11.56	12.8
300	0.55	2.10	5.07	8.20	9.38
400	0.01	1.28	3.69	5.65	6.87
500	0.06	0.91	2.54	4.96	5.38
600	0.29	0.82	2.16	4.13	4.31
700	0.36	0.80	1.89	3.40	3.65
900	0.44	0.83	1.55	2.82	2.74
1100	0.33	0.57	1.04	1.86	1.89
1300	0.44	0.57	1.03	1.79	1.77

The percentage change in absorbed dose conversion factors obtained from source-photons emitted with energies between 30 and 1300 keV are presented in Table 4.10 for LiF dosimeters.These data are presented at depths between 1 and 34 cm for a point source geometry with the source located at phantom center. In these and all other tables, the MCNP reported (in-air) dosimeter calibration values also are presented for reference. It should be noted that, on average, these calibration values agree with their theoretical calculated counterpart (obtained using Eq. 3) to within 1%; no deviation in these data was greater than 4%.

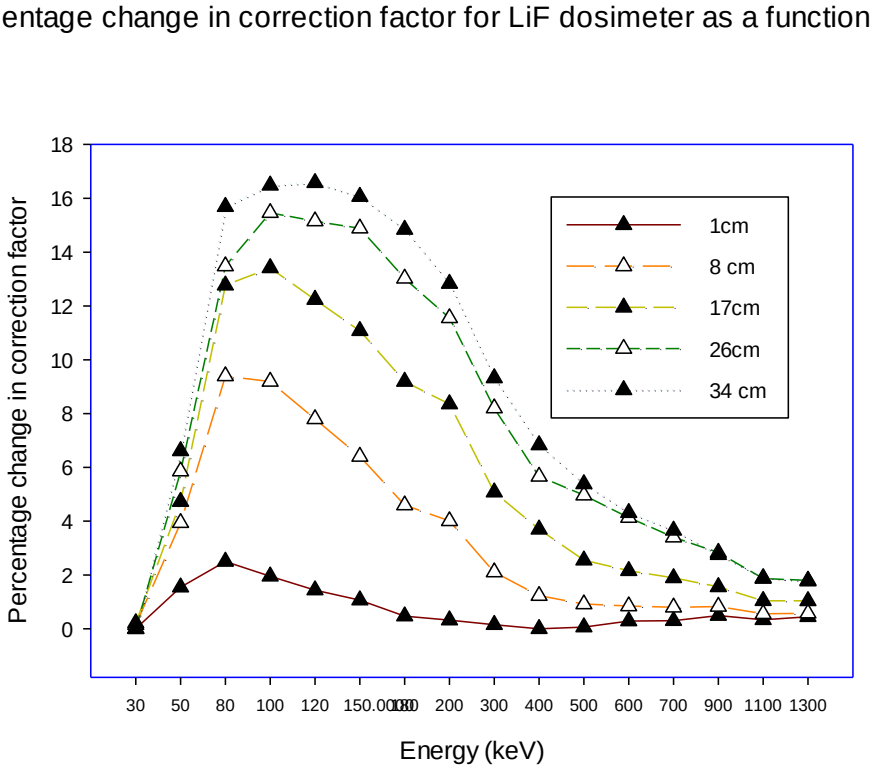

Figure 4.10: Percent deviation of the dosimeter's CF relative to an in-air calibration value for LiF distances of 1, 8, 17, 26, and 34cm in a water phantom. These dosimetric values represent the response from a monoenergetic disk-source located at the surface of a pseudo-infinite water phantom.

Table 4.11: Percentate change in correction factors for Al_2O_3 dosimeters from monoenergetic photons emitted from a disk source located at phantom surface.

Energy			% change in calibration values		
(KeV)			Depth (cm)		
	1	4	8	17	34
30	1.44	1.46	1.48	0	0
50	3.72	11.2	13.9	14.5	14.2
80	12.3	33.3	40.4	43.9	46.3
100	12.1	37.4	47.4	49.9	51.7
120	10.7	34.6	46.0	52.2	56.3
150	8.61	32.6	46.7	55.0	57.5
180	7.75	28.5	44.0	51.1	56.8
200	4.66	24.4	40.5	49.2	52.6
300	2.47	14.9	29.3	40.5	43.9
400	1.81	9.95	23.1	31.8	36.7
500	1.55	7.58	17.3	28.8	30.0
600	1.51	6.07	14.6	23.7	25.0
700	1.45	4.62	9.30	13.4	15.8
900	1.36	4.00	7.04	11.2	13.5
1100	1.11	3.56	4.56	9.50	10.5
1300	0.99	2.71	3.25	8.30	10.9

The percentage change in absorbed dose conversion factors obtained from source-photons emitted with energies between 30and 1300 keV are presented in Table 4.11 for Al dosimeters.These data are presented at depths between 1 and 34 cm for a point source geometry with the source located at phantom center. In these and all other tables, the MCNP reported (in-

air) dosimeter calibration values also are presented for references.

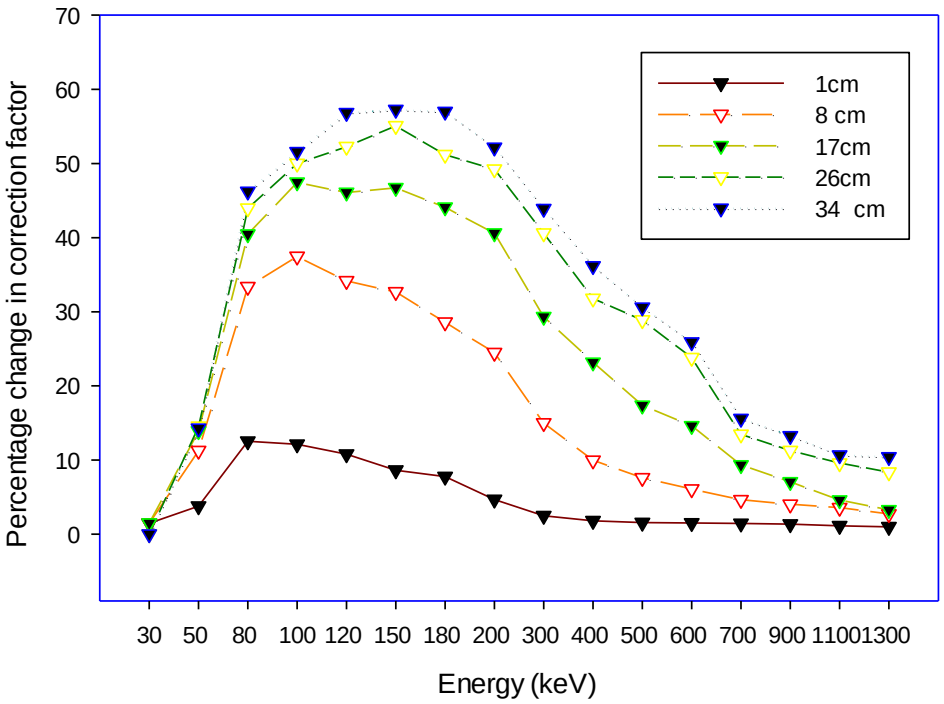

Figure 4.11: Percent deviation of the dosimeter's CF relative to an in-air calibration value for Al distances of 1, 8, 17, 26, and 34cm in a water phantom. These dosimetric values represent the response from a monoenergetic disk-source located at the surface of a pseudo-infinite water phantom.

Table 4.12: Percentate change in correction factors for Si dosimeters from monoenergetic photons emitted from a disk source located at phantom surface.

Energy			% change in calibration values		
(KeV)			Depth (cm)		
30	0.3363	0.3468	0.313	0	0
50	2.64	11.3877	14.49	15.11	16.34
80	15.94	41.43	49.16	52.8	55.07
100	17.8	50.04	60.3	64.19	64.21
120	14.34	49.82	62	67.6	71.49
150	13.57	50.51	65.03	72.27	74.02
180	11.49	45.55	62.99	69.54	74.35
200	8.5606	42.18	60.9	68.97	71.45
300	2.43	27.73	51.51	61.34	64.53
400	1.744	19.33	41.15	52.31	57.24
500	1.33	15.04	32.85	49.17	51.26
600	1.09	11.7	28.2	44	45.3
700	0.84	9.3627	23.68	37.71	39.65
900	0.82	7.08	17.81	31.73	32.4567
1100	2.241	7.17	15.22	26.02	26.17
1300	0.0857	4.41	11.9	21.85	21.78

The percentage change in absorbed dose conversion factors obtained from source-photons emitted with energies between 30 and 1300 keV are presented in Table 4.12 for Si dosimeters.These data are presented at depths between 1 and 34 cm for a point source geometry with the source located at phantom center. In these and all other tables, the MCNP reported (in-air) dosimeter calibration values also are presented for reference. It should be noted that, on average, these calibration values agree with their theoretical calculated counterpart.

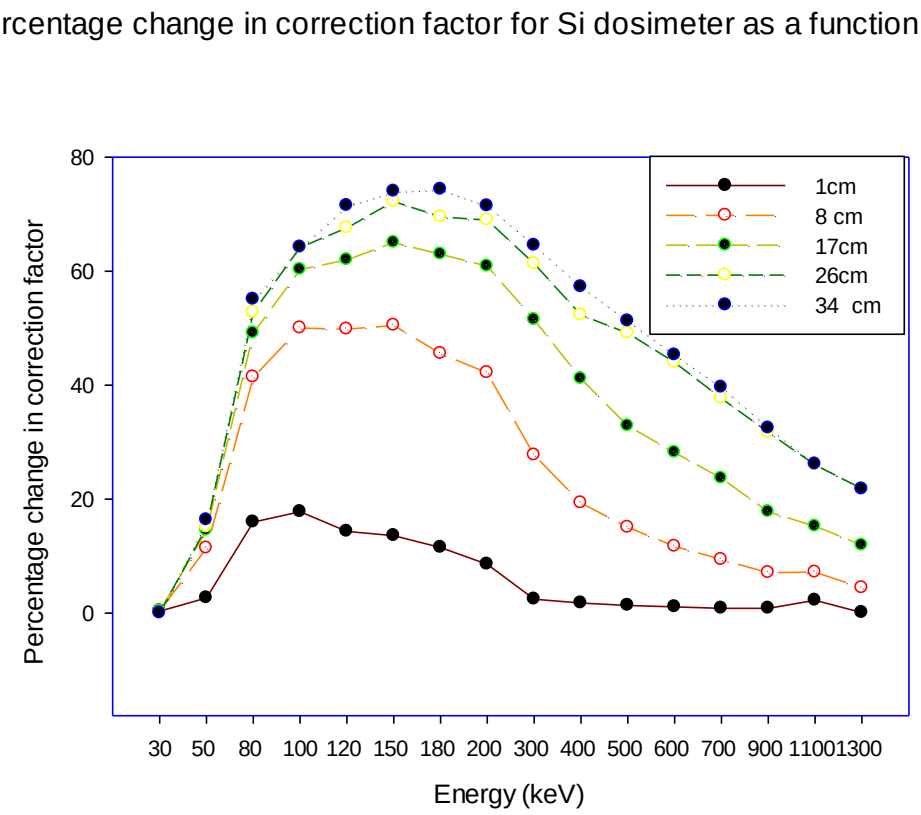

Figure 4.12: Percent deviation of the dosimeter's CF relative to an in-air calibration value for Si distances of 1, 8, 17, 26, and 34cm in a water phantom. These dosimetric values represent the response from a monoenergetic disk-source located at the surface of a pseudo-infinite water phantom.

The dosimeter's tissue correction function for mono-energetic photons and the polyenergetic radionuclides Yb-169 and Ir-192 are compared for LiF, Al_2O_3 and Si dosimeter. The intensity weighted average of the dosimeter correction function from the monoenergetic photons agrees within 5% the polyenergetic photons.

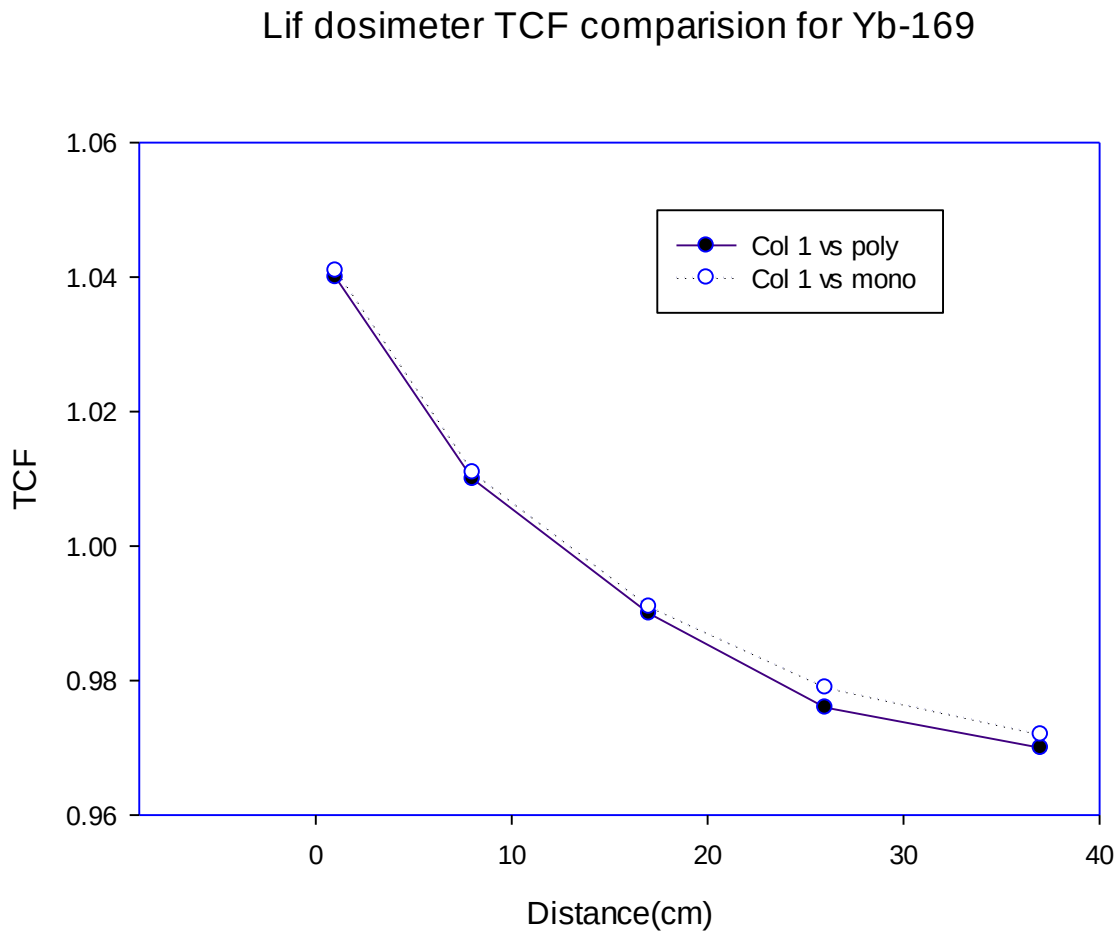

Fig 4.13: Comparison of Tissue correction factor between polyenergetic photon source Yb-169 and the weighted TCF from the monoenergetic sources.

Figs. 4.13, 4.14 and 4.15 show the comparison of tissue correction factor for simulated polyenergetic photon and calculated mono-energetic photon. In each diagram the correction factor for the spectrum (solid line) was contrasted to that of mono-energetic beam (dotted line). Fig 4.13

is the plot of correction values for radionuclide Yb-169 for the dosimeter LiF. Up to 10 cm the TCF values are same for both polyenergetic and mono-energetic photon sources and after 10 cm there is a slight deviation but the values agree within less than 5% which is the AAPM requirement. The graph clearly shows that the tissue correction function for lithium fluoride dosimeter obtained from intensity weighted mono energetic photons is in agreement with simulated polyenergetic Yb-169 spectrum which is the expected result.

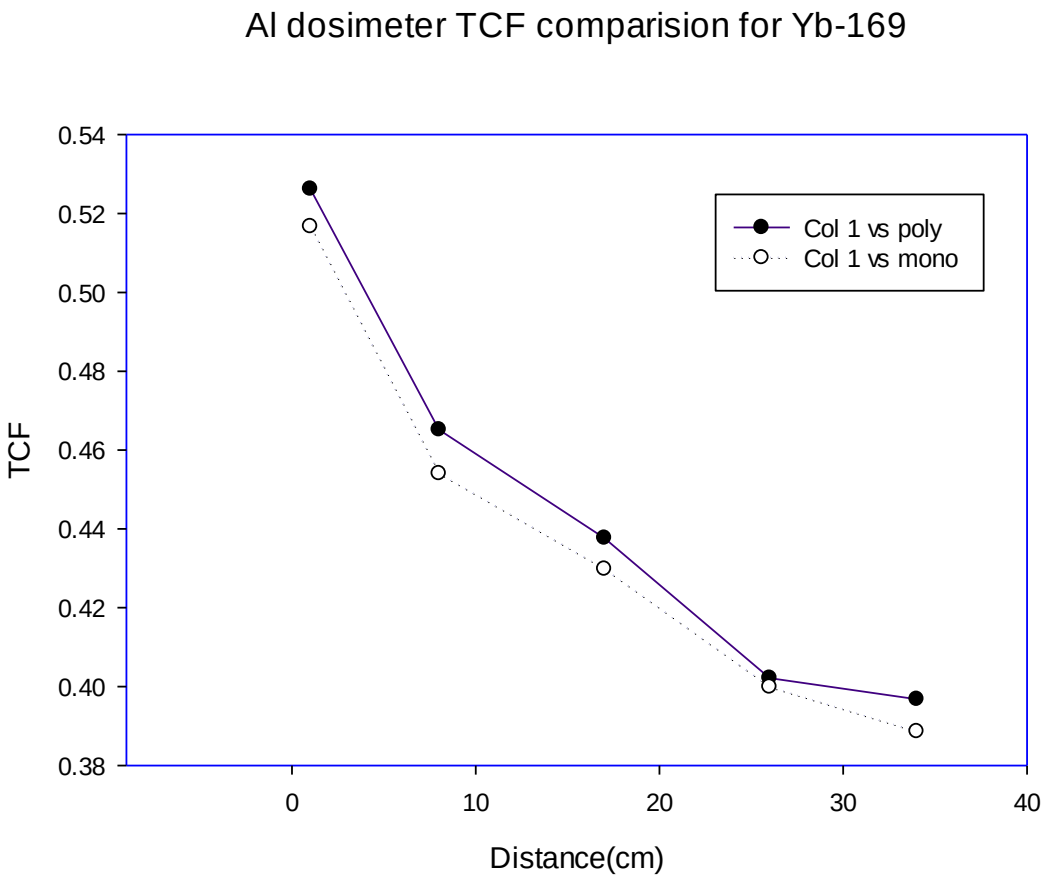

Fig 4.14: Comparison of Tissue correction factor between polyenergetic photon source Yb-169 and the weighted TCF from the monoenergetic sources for Al_2O_3 dosimeter.

In Figure 4.14, the deviation in the dosimeter's calibration value between poly and mono energetic sources at measurement depths up 40 cm is presented for Al_2O_3 dosimeter. Figure shows the calibration curves look similar for both mono-and poly-energetic photons and the calibration values do not exceed the significant deviation of 5% for all measurement depths. The result is in agreement with the author's expectation and fulfill the AAPM requirement.

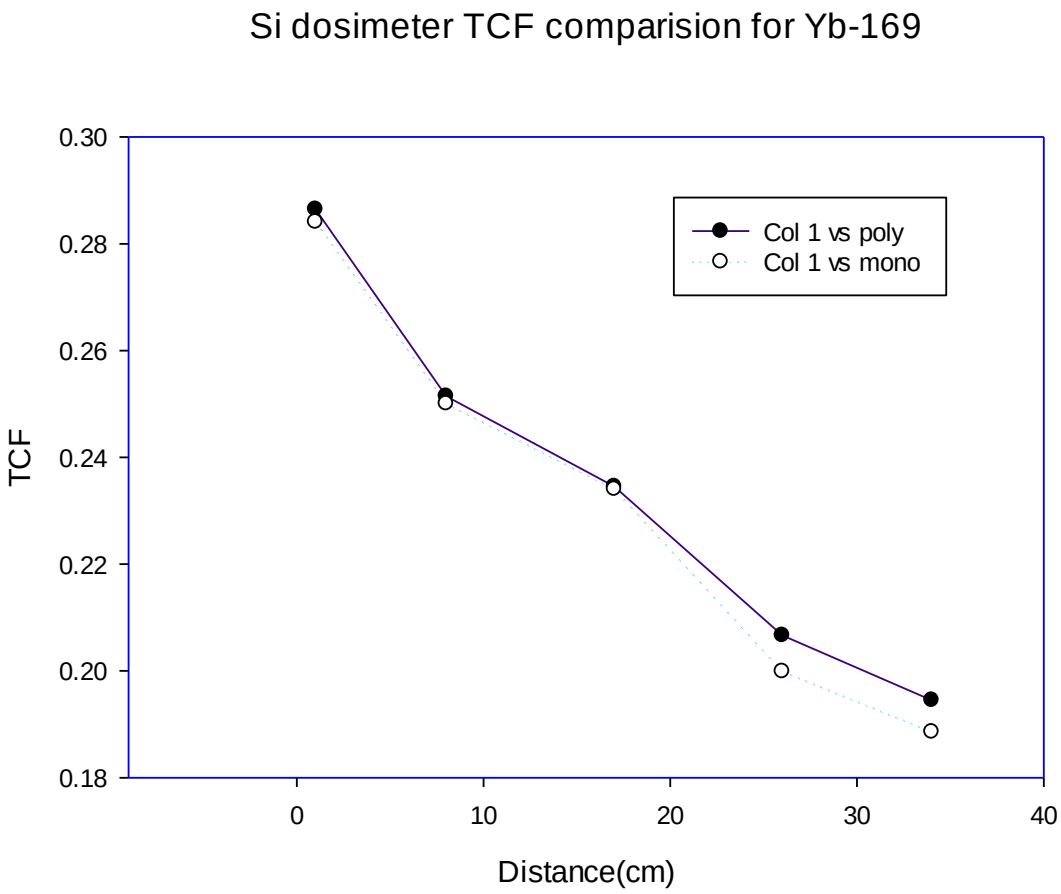

Fig 4.15: Comparison of Tissue correction factor between polyenergetic photon source Yb-169 and the weighted TCF from the monoenergetic sources for Si dosimeter.

In Figure 4.15, the deviation in the dosimeter's calibration value between poly and mono energetic source at measurement depths up 40 cm is presented for Si dosimeter. Calibration values do not exceed the significant deviation of 5% for nearly all measurement depths and two calibration curves look similar which means that the tissue correction function for Si dosimeter from intensity weighted mono energetic photons is in agreement with simulated polyenergetic Yb-169 spectrum which is the expected result.

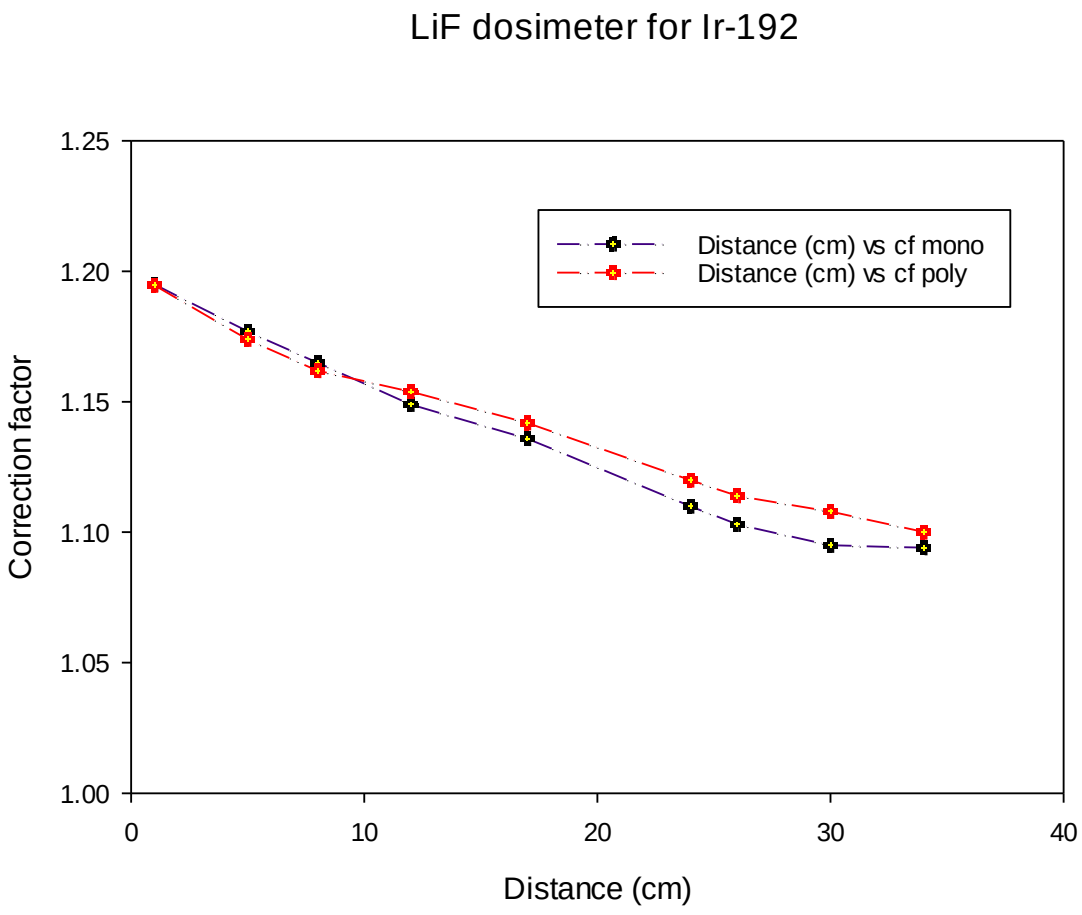

Fig 4.16: Comparison of Tissue correction factor between polyenergetic photon source Ir- 192 and the weighted TCF from the monoenergetic sources for LiF dosimeter.

The deviation in the LiF dosimeter's calibration function between poly and mono energetic sources at measurement depths up 40 cm is presented for radionuclides Ir-192 in figure 4.16. Two calibration curves look similar and the calibration values are within 5 % deviation. The correction function from intensity weighted mono energetic photons is in agreement with simulated polyenergetic Ir-192 spectrum and fulfill the author's expected results.

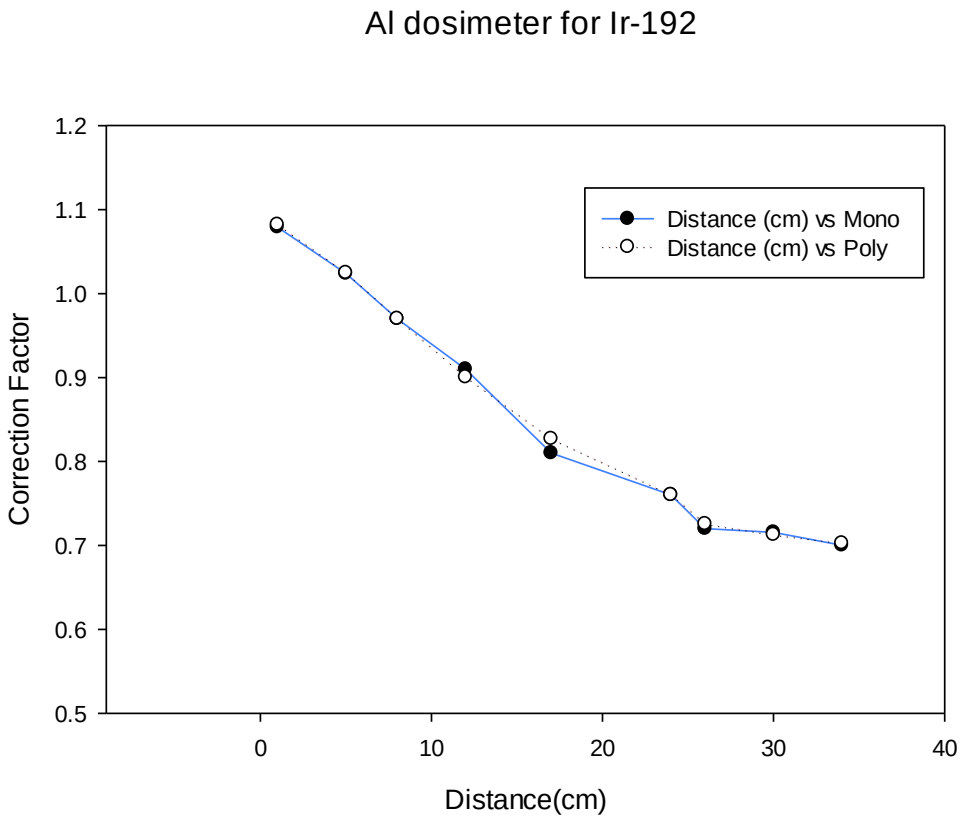

Fig 4.17: Comparison of Tissue correction factor between polyenergetic photon source Ir-192 and the weighted TCF from the monoenergetic sources for Al_2O_3 dosimeter.

In Figure 4.17, the deviation in the Al_2O_3 dosimeter's calibration value between poly and mono energetic sources at measurement depths up 40 cm is presented for radionuclides Ir-192. Again,

calibration values for Al_2O_3 do not exceed the significant deviation of 5% for nearly all measurement depths.The result is in agreement with the author's expectation and fulfill the AAPM requirement.

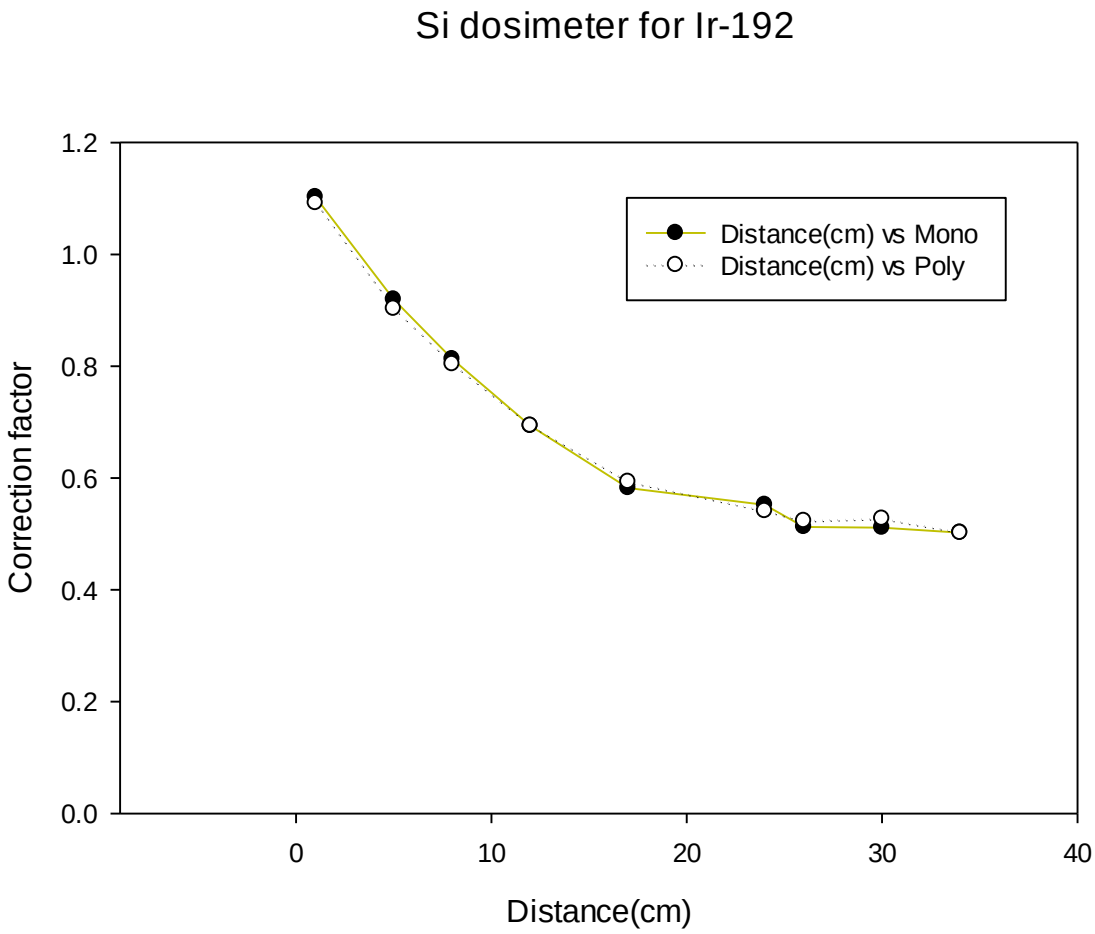

Fig 4.18: Comparison of Tissue correction factor between polyenergetic photon source Ir-192 and the weighted TCF from the monoenergetic sources for Si dosimeter.

In Figure 4.18, the deviation in the Si dosimeter's calibration values between poly and mono energetic source at measurement depths up 40 cm is presented for radionuclides Ir-192. The calibration values do not exceed the significant deviation of 5% for nearly all measurement depths.

The two calibration curves look similar and cf values are almost same up to 10 cm. The result clearly shows the calibration function from intensity weighted mono-energetic photon energies and the simulated poly-energetic source Ir-192 are in agreement with the author's expectations.

5. CONCLUSIONS

The first part of the thesis presents Monte Carlo calculated changes in a LiF, Al_2O_3, and silicon dosimeter's response to monoenergetic 30-300 keV photons as a function of photon energy and depth in water phantom for three common irradiation geometries. In the second part of the thesis, the monoenergetic energy range is extened to 1300 keV and poly-energetic radionuclides for examples Yb-169 and Ir-192 are introduced in order to study the dosimeter's response.Changes in a dosimeter's response at various phantom depths relative to its calibration value, which was obtained under conditions of negligible scatter, were found to exceed the author significant deviation of 5% at depths of 1 cm or greater for Al_2O_3 and silicon and at depths of 7 cm or greater for LiF. Additionally, in these measurements, maximum deviations of 9% were determined for LiF, 43% for Al_2O_3, and 61% for silicon. Maximum deviations were found for primary photons with energies between 100 to 150 keV while minimum deviations were found between 30 to 40 keV. These maximum deviations are attributed to the high photon-scatter probability of primary photons which result in lower-energy (scattered) photons that reach the detector and are more likely to interact through photoelectric absorption; this effect is contrasted with a detectors in-air calibration geometry that is designed to produce and detect a minimal scattered photon fluence. Similarly, the minimum deviations at photon energies between 30 to 40 keV are expected to occur because the majority of these low energy photons are expected to interact directly through photoelectric absorption. Therefore, fewer scattered photon would be expected to be produced which would limit variations in detector response relative to its calibration value.

Additionally, Figs. 4.1, 4.2, and 4.3 also demonstrate how the irradiation geometry can modify detector response. As an example, when the silicon dosimeter was simulated to determine the

dosimetric output of a point-source placed at the center of a water phantom, the maximum deviation between the dosimeter calibration value and its response was 61%. Yet when the geometry was modified such that the source was placed at the phantom surface, the maximum deviation from its calibration value was determined to be 53%. Similarly for the 10 cm radial field geometry, the maximum deviation from calibration was 47%. This difference is attributed to the effectiveness of the central point-source geometry in creating scattered photons that then are detected by the dosimeter.

Lastly, the data is used to obtain a dosimeter CF for poly-energetic photon sources (Yb-169 and Ir-192) by taking a photon-intensity weighted average of the dosimeter conversion factor of each photon energy at the dosimeter measurement depth and for the field source irradiation geometry. Since we have taken in to account both the spectral qualities of the beam and the material through which it passes, the difference in a dosimeter CF for poly-and mono- energetic photon is within 5 % which fulfill the AAPM requirement.Although, while this is an effective method for calculating dosimeter CFs, better accuracy can be achieved by performing an in-depth Monte Carlo analysis in which the actual design of the source is simulated [48, 54].

6. References

1. Briesmeister, J.F., *MCNPTM-A general Monte Carlo N-particle transport code.*

2. Holloway, A. and E.M. Campbell, *A Lithium Fluoride Thermoluminescent Dosimeter*, in *Symposium on High-Energy Electrons*, A. Zuppinger and G. Poretti, Editors. 1965, Springer Berlin Heidelberg. p. 61-65.

3. Khan, F.M., *The physics of radiation therapy*. 4th ed. 2010: Lippincott Williams & Wilkins.

4. Oliveira, F.F., et al., *In vivo dosimetry with silicon diodes in total body irradiation.* Radiation Physics and Chemistry, 2014. **95**(0): p. 230-232.

5. Hu, B., Y. Wang, and W. Zealey, *Performance of Al2O3:C optically stimulated luminescence dosimeters for clinical radiation therapy applications.* Australasian Physical & Engineering Sciences in Medicine, 2009. **32**(4): p. 226-232.

6. Cunningham, H.E.J.a.J.R., *The Physics of Radiology*, ed. 4th. 1983, Springfield: Charles C. Thosmas.

7. Cember, H., *Introduction to Health Physics*. Third ed. 1996: McGraw-Hill. 733.

8. Attix, F.H., *Introduction to Radiological Physics*. 2004, New York, NY: Wiley VCH. 607.

9. Hubbell, J.H. and S.M. Seltzer. *Tables of x-ray mass attenuation coefficients and mass energy-absorption coerricients (version 1.03)*. 2010; Available from: http://physics.nist.gov/PhysRefData/XrayMassCoef/cover.html.

10. Perez-Calatayud, J., D. Granero, and F. Ballester, *Phantom size in brachytherapy source dosimetric studies.* Med Phys, 2004. **31**(7): p. 2075-81.

11. Knoll, G.F., *Radiation Detection and Measurement*. 4th Edition ed. 2010, New York: Wiley. 860.

12. Nath, R., et al., *Code of practice for brachytherapy physics: report of the AAPM Radiation Therapy Committee Task Group No. 56.* Medical physics, 1997. **24**(10): p. 1557-1598.

13. Sen, S., D. Salie, and E. Tomchuk, *The Decay of 169Yb.* Canadian Journal of Physics, 1972. **50**(19): p. 2348-2354.

14. Pakravan, D., M. Ghorbani, and A.S. Meigooni, *Evaluation of 101Rh as a brachytherapy source.* Journal of contemporary brachytherapy, 2015. **7**(2): p. 171.

15. Leonard, K.L., et al., *A novel ytterbium-169 brachytherapy source and delivery system for use in conjunction with minimally invasive wedge resection of early-stage lung cancer.* Brachytherapy, 2011. **10**(2): p. 163-169.

16. Hayward, P. and D. Currie, *Radiography Of Welds Using Selenium 75, Ir 192 And X-Rays.* 12th A-PCNDT, 2006.

17. Palmer, A., O. Hayman, and S. Muscat, *Treatment planning study of the 3D dosimetric differences between Co-60 and Ir-192 sources in high dose rate (HDR) brachytherapy for cervix cancer.* Journal of contemporary brachytherapy, 2012. **4**(1): p. 52.

18. Liu, Y., et al., *Dynamic rotating-shield brachytherapy.* Medical physics, 2013. **40**(12): p. 121703.

19. Ghorbani, M., et al., *Effect of tissue composition on dose distribution in brachytherapy with various photon emitting sources.* Journal of contemporary brachytherapy, 2014. **6**(1).

20. Zaman, Z., et al., *Comparison of planned and measured rectal dose in-vivo during high dose rate Cobalt-60 brachytherapy of cervical cancer.* Physica Medica, 2014. **30**(8): p. 980-984.

21. Wang, R., et al., *Implementation of GaN based real-time source position monitoring in HDR brachytherapy.* Radiation Measurements, 2014. **71**: p. 293-296.

22. Bushberg, J.T., et al., *The Essential Physics of Medical Imaging*. 2011: Wolters Kluwer Health.

23. Huda, W., *Review of Radiologic Physics*. 2016: Lippincott Williams & Wilkins.

24. Smith-Bindman, R., et al., *Radiation dose associated with common computed tomography examinations and the associated lifetime attributable risk of cancer.* Archives of internal medicine, 2009. **169**(22): p. 2078-2086.

25. Moussa, H.M., K.F. Eckerman, and L.W. Townsend, *Charged particle equilibrium effects on the electron absorbed fraction in the extrathoracic airways.* Radiat Prot Dosimetry, 2006. **121**(3): p. 252-6.

26. Seuntjens, J., W. Strydom, and K. Shortt, *Dosimetric principles, quantities and units.* Radiation oncology physics: a handbook for teachers and students. Podgorsak EB, editor. Vienna, Austria: IAEA, 2005.

27. Seuntjens, J., W. Strydom, and K. Shortt, *Dosimetric principles, quantities and units.*

28. Okuno, E., . *Fundamentals of Dosimetry*.

29. Bielajew, A.F., *Fundamentals of Radiation Dosimetry and Radiological Physics.* 2005.

30. Choi, J. and J.O. Kang, *Basics of particle therapy II: relative biological effectiveness.* Radiation oncology journal, 2012. **30**(1): p. 1-13.

31. Hirning, C.R., *Detection and determination limits for thermoluminescence dosimetry.* Health Phys, 1992. **62**(3): p. 223-7.

32. Del Sol Fernández, S., et al., *Thermoluminescent characteristics of LiF:Mg, Cu, P and CaSO4:Dy for low dose measurement.* Applied Radiation and Isotopes, 2016. **111**: p. 50-55.

33. Faulkner, K., P. Ortiz-Lopez, and E. Vano, *Patient dosimetry in diagnostic and interventional radiology: a practical approach using trigger levels.* Radiation protection dosimetry, 2005. **117**(1-3): p. 166-168.

34. Mettler Jr, F.A., et al., *Effective Doses in Radiology and Diagnostic Nuclear Medicine: A Catalog 1*. Radiology, 2008. **248**(1): p. 254-263.

35. Brambilla, M., et al., *Patient radiation doses and references levels in interventional radiology*. Radiol Med, 2004. **107**(4): p. 408-18.

36. Huda, W. and N.A. Gkanatsios, *Effective dose and energy imparted in diagnostic radiology*. Medical physics, 1997. **24**(8): p. 1311-1316.

37. Gkanatsios, N.A. and W. Huda, *Computation of energy imparted in diagnostic radiology*. Medical physics, 1997. **24**(4): p. 571-579.

38. Shah, D., R. Sachs, and D. Wilson, *Radiation-induced cancer: a modern view*. The British journal of radiology, 2014.

39. Shultis, J.K. and R.E. Faw, *An MCNP primer*.

40. Munoz, A., et al., *Monte Carlo Methods to Model Radiation Interactions and Induced Damage*, in *Radiation Damage in Biomolecular Systems*. 2012, Springer. p. 203-225.

41. Salvat, F., J.M. Fernández-Varea, and J. Sempau. *PENELOPE-2006: A code system for Monte Carlo simulation of electron and photon transport*.

42. Kawrakow, I. *The monte carlo simulation of radiation transport*.

43. Reed, A.L., *Medical physics calculations with MCNP: a primer*. 2007.

44. Shultis, J.K. and R.E. Faw, *An MCNP primer*.

45. Briesmeister, J., *MCNP5 - A General Monte Carlo N-particle Transport Code, Version 5 LA-03-1987*. 2008.

46. Cullen, D.E., J.H. Hubbell, and L. Kissel, *EPDL97: the evaluated photon data library,'97 version.* 1997.

47. Turner, J.E., *Atoms, radiation, and radiation protection*. 2008: John Wiley & Sons.

48. Ariel E. Hirsch, M., et al., *Polymethylmethacrylate and Radioisotopes in Vertebral Augmentation: An Explanation of Underlying Principles.* Pain Physician, 2009. **12**(5): p. 887-891.

49. Berger, M.J., J.S. Coursey, and M.A. Zucker. *Stopping-Power and Range Tables for Electrons, Protons, and Helium Ions*. 2000; Available from: http://physics.nist.gov/PhysRefData/Star/Text/contents.html.

50. Firestone, R., *Nuclear structure and decay data in the electronic age.* Journal of Radioanalytical and Nuclear Chemistry, 2000. **243**(1): p. 77-86.

51. Rivard, M.J., et al., *Update of AAPM Task Group No. 43 Report: A revised AAPM protocol for brachytherapy dose calculations.* Medical physics, 2004. **31**(3): p. 633-674.

52. Paul, R. and R. Lindstrom, *Prompt gamma-ray activation analysis: fundamentals and applications.* Journal of Radioanalytical and Nuclear Chemistry, 2000. **243**(1): p. 181-189.

53. Medich, D.C. and J.J. Munro, *Dependence of Yb-169 absorbed dose energy correction factors on self-attenuation in source material and photon buildup in water.* Medical physics, 2010. **37**(5): p. 2135-2144.

54. Medich, D.C. and J.J. Munro, *Dependence of Yb-169 absorbed dose energy correction factors on self-attenuation in source material and photon buildup in water.* Medical Physics, 2010. **37**(5): p. 2135-2144.

7. APPENDIX: MCNP6 INPUT FILE

For Yb-169

```
Tissue correction factor deck (yb-169)
c used to analyze the tissue to dose correction factors
c as a fucntion of depth in a water phantom
c for LiF, Al2O3, and Si dosimeters for Polyenergetic
c source.
c written by
c s poudel
c February 19, 2016
c
c
c Cell cards
c
1     1   -1.00 (-10)     imp: p, e=1 $water phantom
2     0         (10 -20) imp: p, e=1 $void around phantom
100   0         (20)      imp: p, e=0 $end of the world


c
c Surface cards
c box 40 cm deep, face-centered at origin, 80 cm tall and wide
10 Box 0 -40 -40   40 0 0   0 80 0   0 0 80
c
```

c end of the world

20 so 100 $ end of the world

c data cards

Mode p

c

c TALLY SECTION

c tally flux from 0 to 10 cm deep using F

MESH tally

c also use the DE/DF cards to convert flux

c into dose using electron stopping power

c

c WATER tally

*FMESH04: p Geom = xyz Origin = -0.05 -0.05 -0.05

IMESH = 35.05 IINTS = 351

JMESH = 0.05 JINTS = 1

KMESH = 0.05 KINTS = 1

OUT = col

c Convert flux ($1/cm^2$) to water dose (MeV/g) using

c the H_2O DE/DF mass energy absorptions constants

DE04 DF04

2.00E-02 5.50E-01

3.00E-02 1.56E-01

4.00E-02 6.95E-02

5.00E-02 4.22E-02

6.00E-02 3.19E-02

8.00E-02 2.60E-02

1.00E-01 2.55E-02

1.50E-01 2.76E-02

2.00E-01 2.97E-02

3.00E-01 3.19E-02

4.00E-01 3.28E-02

5.00E-01 3.30E-02

6.00E-01 3.28E-02

8.00E-01 3.21E-02

1.00E+00 3.10E-02

c

c LiF Mesh tally

*FMESH14: p Geom = xyz Origin = -0.05 -0.05 -0.05

IMESH = 35.05 IINTS = 351

JMESH = 0.05 JINTS = 1

KMESH = 0.05 KINTS = 1

OUT = col

c Convert flux (1/cm2) to LiF dose (MeV/g) using

c the LiF DE/DF mass energy absorptions constants

c

DE14 DF14

2.00E-02 6.49E-01

3.00E-02 1.83E-01

4.00E-02 7.89E-02

5.00E-02 4.54E-02

6.00E-02 3.22E-02

8.00E-02 2.39E-02

1.00E-01 2.23E-02

1.50E-01 2.33E-02

2.00E-01 2.48E-02

3.00E-01 2.66E-02

4.00E-01 2.73E-02

5.00E-01 2.75E-02

6.00E-01 2.74E-02

8.00E-01 2.67E-02

1.00E+00 2.59E-02

c

c Al2O3 Mesh tally

*FMESH24: p Geom = xyz Origin = -0.05 -0.05 -0.05

IMESH = 35.05 IINTS = 351

JMESH = 0.05 JINTS = 1

KMESH = 0.05 KINTS = 1

OUT = col

c Convert flux (1/cm^2) to Al_2O_3 dose (MeV/g) using

c the Al_2O_3 DE/DF mass energy absorptions constants

c

# DE24	DF24
2.00E-02	1.96E+00
3.00E-02	5.55E-01
4.00E-02	2.30E-01
5.00E-02	1.20E-01
6.00E-02	7.43E-02
8.00E-02	4.13E-02
1.00E-01	3.15E-02
1.50E-01	2.70E-02
2.00E-01	2.74E-02
3.00E-01	2.87E-02
4.00E-01	2.93E-02
5.00E-01	2.95E-02
6.00E-01	2.93E-02
8.00E-01	2.86E-02
1.00E+00	2.76E-02

c

c c SILICON Mesh tally

*FMESH34: p Geom = xyz Origin = -0.05 -0.05 -0.05

IMESH = 35.05 IINTS = 351

```
        JMESH = 0.05   JINTS = 1
        KMESH = 0.05   KINTS = 1
        OUT = col
c Convert flux (1/cm2) to SILICON dose (MeV/g) using
c the Si DE/DF mass energy absorptions constants
c
#    DE34          DF34
     2.00E-02      4.08E+00
     3.00E-02      1.16E+00
     4.00E-02      4.78E-01
     5.00E-02      2.43E-01
     6.00E-02      1.43E-01
     8.00E-02      6.90E-02
     1.00E-01      4.51E-02
     1.50E-01      3.09E-02
     2.00E-01      2.91E-02
     3.00E-01      2.93E-02
     4.00E-01      2.97E-02
     5.00E-01      2.97E-02
     6.00E-01      2.95E-02
     8.00E-01      2.88E-02
     1.00E+00      2.78E-02
c end tally section
```

```
c
c SOURCE DEFINITION SECTION for Yb-92
c source is a MONODIRECTIONAL PHOTON DISC SOURCE
c
c
SDEF Par=2 pos=-1 0 0 axs=1 0 0 ext=0 erg=d2 rad=d1
c
SI1 0 0.5    $create a disc with 1 cm diameter
SP1 -21 1    $uniform radial sampling within disk
C Energies and probabilities
si2   l   0.0495 0.0507 0.0576 0.0591 0.0631 &
        0.0936 0.1098 0.1182 0.1305 0.1772 0.1980 0.2611 0.3077
sp2   d   0.5320 0.9400 0.2950 0.0820 0.4420 &
        0.0260 0.1750 0.0190 0.1130 0.2220 0.3580 0.0170 0.1010
c end source term definitions
c
c MATERIAL DEFINITION SECTION
c Define the material(s) present in the model
c water
m1    1000 0.6666 8000 0.3334
c end material definitions
c
nps 40000000000
```

For Ir-192

Tissue correction factor deck (Am-241)

```
c used to analyze the tissue to dose correction factors
c as a fucntion of depth in a water phantom
c for LiF, Al2O3, and Si dosimeters for Polyenergetic
c source I-125.
c written by
c s poudel
c February 19, 2016
c
c
c Cell cards
c
1     1   -1.00 (-10)     imp: p, e=1 $water phantom
2     0         (10 -20) imp: p, e=1 $void around phantom
100   0         (20)      imp: p, e=0 $end of the world

c
c Surface cards
c box 40 cm deep, face-centered at origin, 80 cm tall and wide
10 Box 0 -40 -40   40 0 0   0 80 0   0 0 80
c
```

```
c end of the world
20 so 100 $ end of the world


c data cards
Mode p
c
c TALLY SECTION
c tally flux from 0 to 10 cm deep using F
MESH tally
c also use the DE/DF cards to convert flux
c into dose using electron stopping power
c
c WATER tally
*FMESH04: p Geom = xyz Origin = -0.05 -0.05 -0.05
          IMESH = 35.05   IINTS = 351
          JMESH = 0.05   JINTS = 1
          KMESH = 0.05   KINTS = 1
          OUT = col
c Convert flux (1/cm2) to water dose (MeV/g) using
c the H2O DE/DF mass energy absorptions constants
#    DE04      DF04
         2.00E-02              5.50E-01
         3.00E-02              1.56E-01
```

4.00E-02 6.95E-02

5.00E-02 4.22E-02

6.00E-02 3.19E-02

8.00E-02 2.60E-02

1.00E-01 2.55E-02

1.50E-01 2.76E-02

2.00E-01 2.97E-02

3.00E-01 3.19E-02

4.00E-01 3.28E-02

5.00E-01 3.30E-02

6.00E-01 3.28E-02

8.00E-01 3.21E-02

1.00E+00 3.10E-02

c

c LiF Mesh tally

*FMESH14: p Geom = xyz Origin = -0.05 -0.05 -0.05

IMESH = 35.05 IINTS = 351

JMESH = 0.05 JINTS = 1

KMESH = 0.05 KINTS = 1

OUT = col

c Convert flux (1/cm^2) to LiF dose (MeV/g) using

c the LiF DE/DF mass energy absorptions constants

c

DE14 DF14

2.00E-02 6.49E-01

3.00E-02 1.83E-01

4.00E-02 7.89E-02

5.00E-02 4.54E-02

6.00E-02 3.22E-02

8.00E-02 2.39E-02

1.00E-01 2.23E-02

1.50E-01 2.33E-02

2.00E-01 2.48E-02

3.00E-01 2.66E-02

4.00E-01 2.73E-02

5.00E-01 2.75E-02

6.00E-01 2.74E-02

8.00E-01 2.67E-02

1.00E+00 2.59E-02

c

c Al2O3 Mesh tally

*FMESH24: p Geom = xyz Origin = -0.05 -0.05 -0.05

IMESH = 35.05 IINTS = 351

JMESH = 0.05 JINTS = 1

KMESH = 0.05 KINTS = 1

OUT = col

c Convert flux (1/cm2) to Al_2O_3 dose (MeV/g) using

c the Al_2O_3 DE/DF mass energy absorptions constants

c

#	DE24	DF24
	2.00E-02	1.96E+00
	3.00E-02	5.55E-01
	4.00E-02	2.30E-01
	5.00E-02	1.20E-01
	6.00E-02	7.43E-02
	8.00E-02	4.13E-02
	1.00E-01	3.15E-02
	1.50E-01	2.70E-02
	2.00E-01	2.74E-02
	3.00E-01	2.87E-02
	4.00E-01	2.93E-02
	5.00E-01	2.95E-02
	6.00E-01	2.93E-02
	8.00E-01	2.86E-02
	1.00E+00	2.76E-02

c

c c SILICON Mesh tally

*FMESH34: p Geom = xyz Origin = -0.05 -0.05 -0.05

IMESH = 35.05 IINTS = 351

JMESH = 0.05 JINTS = 1

KMESH = 0.05 KINTS = 1

OUT = col

c Convert flux (1/cm2) to SILICON dose (MeV/g) using

c the Si DE/DF mass energy absorptions constants

c

# DE34	DF34
2.00E-02	4.08E+00
3.00E-02	1.16E+00
4.00E-02	4.78E-01
5.00E-02	2.43E-01
6.00E-02	1.43E-01
8.00E-02	6.90E-02
1.00E-01	4.51E-02
1.50E-01	3.09E-02
2.00E-01	2.91E-02
3.00E-01	2.93E-02
4.00E-01	2.97E-02
5.00E-01	2.97E-02
6.00E-01	2.95E-02
8.00E-01	2.88E-02
1.00E+00	2.78E-02

c end tally section

```
c
c SOURCE DEFINITION SECTION for Ir-92
c source is a MONODIRECTIONAL PHOTON DISC SOURCE
c
c
SDEF Par=2 pos=-1 0 0 axs=1 0 0 ext=0 erg=d2 rad=d1
c
SI1 0 0.5    $create a disc with 1 cm diameter
SP1 -21 1    $uniform radial sampling within disk
C Energies and probabilities
#       SI2          SP2
        L            D
      0.061486     0.012000
      0.063000     0.020500
      0.065122     0.026300
      0.066831     0.044600
      0.071079     0.002410
      0.071414     0.004660
      0.073363     0.001630
      0.075368     0.005330
      0.075749     0.010250
      0.077831     0.003650
      0.110400     0.000122
```

0.136343	0.002000
0.176980	0.000043
0.201311	0.004730
0.205794	0.033400
0.280270	0.000090
0.283267	0.002660
0.295957	0.287200
0.308455	0.296800
0.316506	0.827100
0.329170	0.000174
0.374485	0.007260
0.416469	0.006690
0.420520	0.000690
0.468069	0.478100
0.484575	0.031870
0.485300	0.000023
0.489060	0.004380
0.588581	0.045170
0.593490	0.000421
0.599410	0.000039
0.604411	0.082000
0.612462	0.053400
0.703870	0.000053

```
      0.765800     0.000013
      0.884537     0.002910
      1.061480     0.000530
      1.089900     0.000012
      1.378200     0.000012
c end source term definitions
c
c MATERIAL DEFINITION SECTION
c Define the material(s) present in the model
c water
m1    1000 0.6666 8000 0.3334
c end material definitions
c
nps 4000000000
```